MATERIALS SCIENCE

Battery-free, skin-interfaced microfluidic/electronic systems for simultaneous electrochemical, colorimetric, and volumetric analysis of sweat

Amay J. Bandodkar[1,2]*, Philipp Gutruf[1,2,3]*, Jungil Choi[1,2]*, KunHyuck Lee[1], Yurina Sekine[4], Jonathan T. Reeder[1,2], William J. Jeang[1,2], Alexander J. Aranyosi[2,5], Stephen P. Lee[2,5], Jeffrey B. Model[2,5], Roozbeh Ghaffari[2,5,6], Chun-Ju Su[1], John P. Leshock[6], Tyler Ray[1,2], Anthony Verrillo[1], Kyle Thomas[7], Vaishnavi Krishnamurthi[8], Seungyong Han[9], Jeonghyun Kim[10], Siddharth Krishnan[1,11,12], Tao Hang[13], John A. Rogers[1,2,5,10,11,14,15,16,17,18]†

Wearable sweat sensors rely either on electronics for electrochemical detection or on colorimetry for visual readout. Non-ideal form factors represent disadvantages of the former, while semiquantitative operation and narrow scope of measurable biomarkers characterize the latter. Here, we introduce a battery-free, wireless electronic sensing platform inspired by biofuel cells that integrates chronometric microfluidic platforms with embedded colorimetric assays. The resulting sensors combine advantages of electronic and microfluidic functionality in a platform that is significantly lighter, cheaper, and smaller than alternatives. A demonstration device simultaneously monitors sweat rate/loss, pH, lactate, glucose, and chloride. Systematic studies of the electronics, microfluidics, and integration schemes establish the key design considerations and performance attributes. Two-day human trials that compare concentrations of glucose and lactate in sweat and blood suggest a potential basis for noninvasive, semi-quantitative tracking of physiological status.

INTRODUCTION

Thin, soft wearable sensors that intimately integrate with the human body offer unique capabilities in continuous, clinical quality recording of vital physiological parameters, with potential to transform modalities for health and performance monitoring (*1*–*3*). Recent advances in materials engineering (*4*), mechanics (*5*), and electronics (*6*) establish the foundations for stretchable (*7*, *8*) and flexible (*9*) sensors that can conform to the complex, textured surface of skin. The results enable high precision sensing through an intimate skin interface, without irritation or discomfort. Much research in this area focuses on monitoring of physiologic and kinematic parameters related to body movements (*10*), oxygen saturation (*11*), biopotentials (*12*), surface pressure (*13*), temperature and thermal transport properties (*14*), stress/strain and elastic modulus (*15*), blood flow (*16*), and hydration (*17*). Comparatively less emphasis is on real-time and noninvasive measurements of chemical biomarkers (*18*–*21*). Recent reports demonstrate that the collection and chemical analysis of sweat can provide noninvasive means for tracking physiologically relevant electrolytes, metabolites, and small molecules (*20*, *21*). Studies suggest that sweat lactate is an indicator of physical stress and can help to identify transitions from aerobic to anaerobic states (*22*–*24*) and that sweat glucose can serve, at least qualitatively, as a means for tracking blood glucose levels (*25*–*27*). Similarly, sweat chloride (*28*), pH (*29*), and average sweat rate (*30*) provide important insights into electrolyte balance, hydration status, and overall health. Each of these parameters can therefore separately define certain specific conditions of the human body. However, simultaneous analyses of all parameters can offer improved insights into the physiological state. In addition, the pH of sweat can affect the signals of enzyme-based electrochemical sensors. Hence, the integrated pH sensor can inform adjustments in interpreting the response of the enzymatic sensors to accurately quantify sweat glucose and lactate.

Conventional methodologies for sweat analysis involve collection using gauze pads taped to the skin, followed by chemical compositional determination using benchtop instruments. Although useful in laboratory and clinical contexts, these approaches cannot provide real-time information, and their accuracy is limited by loss, contamination, and degradation of samples during the multistep processes of collection, storage, transport, and analysis. Alternative strategies exploit body-worn sensors for real-time, on-skin analysis using electrochemical potentiometric and amperometric techniques (*2*, *20*). These approaches, however, involve complex collections of hardware: potentiostats for signal generation, Bluetooth radios for data transmission, and rechargeable batteries for power supply. Because these subsystems are difficult to miniaturize, they dominate the overall form factor (*12*, *20*, *31*) in a way that leads to nonideal size and weight for mounting on the skin. In addition, potentiometric electrolytic sensors require preconditioning in

[1]Department of Materials Science and Engineering, Northwestern University, Evanston, IL 60208, USA. [2]Center for Bio-Integrated Electronics, Simpson Querrey Institute for BioNanotechnology, Northwestern University, Evanston, IL 60208, USA. [3]Department of Biomedical Engineering, University of Arizona, Tucson, AZ 85721, USA. [4]Materials Sciences Research Center, Japan Atomic Energy Agency Tokai, Ibaraki 319-1195, Japan. [5]Epicore Biosystems Inc., Cambridge, MA 02139, USA. [6]Department of Biomedical Engineering, Northwestern University, Evanston, IL 60208, USA. [7]Department of Biomedical Engineering, Washington University in St. Louis, St. Louis, MO 63130, USA. [8]Functional Material and Microsystems Research Group and Micro Nano Research Facility, RMIT University, Melbourne, Victoria 3000, Australia. [9]Department of Mechanical Engineering, Ajou University, San 5, Woncheon-Dong, Yeongtong-Gu, Suwon 16499, Republic of Korea. [10]Department of Electronics Convergence Engineering, Kwangwoon University, Seoul 01897, Republic of Korea. [11]Department of Materials Science and Engineering, University of Illinois at Urbana-Champaign, Urbana, IL 61801, USA. [12]Frederick Seitz Materials Research Laboratory, University of Illinois at Urbana-Champaign, Urbana, IL 61801, USA. [13]State Key Laboratory of Metal Matrix Composites, School of Materials Science and Engineering, Shanghai Jiao Tong University, Shanghai 200240, P. R. China. [14]Feinberg School of Medicine, Northwestern University, Evanston, IL 60208, USA. [15]Department of Electrical Engineering and Computer Science, Northwestern University, Evanston, IL 60208, USA. [16]Department of Neurological Surgery, Northwestern University, Evanston, IL 60208, USA. [17]Department of Chemistry, Northwestern University, Evanston, IL 60208, USA. [18]Department of Mechanical Engineering, Northwestern University, Evanston, IL 60208, USA.
*These authors contributed equally to this work.
†Corresponding author. Email: jrogers@northwestern.edu

standard solutions and calibration before use, commonly with challenges in uncontrolled drifts in signal (*32*). Potentiometric sensors that use wireless, battery-free electronics are promising as alternatives, but they can only sense electrolyte levels and fail to detect other physiologically relevant species such as metabolites, proteins, and drugs (*33*). Reported designs also have limited ability to accurately capture dynamic changes in sweat due to lack of controlled routing of freshly excreted sweat to the surfaces of the sensors. In this context, colorimetric sensors deployed in thin, soft microfluidic networks that guide and route sweat into compartmentalized microchambers optimally configured for measurement and readout are appealing (*21*). Although these systems have the additional advantage that they can capture well-defined volumes of sweat and quantify the sweat rate and total sweat loss, colorimetric reagents are available only for a modest set of sweat biomarkers.

Here, we present ideas for electrochemical sensing in a mode where target analytes spontaneously generate electrical signals proportional to their concentration, much like the operation of a biofuel cell (*34*, *35*). This approach eliminates the need for a potentiostat, thereby markedly simplifying the electronics compared to those required for conventional amperometric sensors. As a result, miniaturized, low-cost modules based on near-field communication (NFC) technology can be used for the entire range of sensing and communication functions. A magnetically releasable mechanical/electrical interface joins reusable systems of this type with single-use microfluidic platforms that can also embed colorimetric reagents. The outcome is a hybrid colorimetric/biofuel cell system in a thin, skin-compatible form factor, with accurate, multifunctional modes of operation. A demonstrator device illustrates real-time sensing of the concentration of chloride, lactate, and glucose, simultaneously with pH, sweat rate, and total sweat loss. The collective physiological relevance of these parameters allows for comprehensive tracking of health status. Here, the eccrine glands themselves provide pressure for routing sweat through a network of microfluidic channels and valves designed to interface with an individual, separately located sensors in a way that eliminates contamination and cross-talk.

Commercial interstitial fluid-based glucose sensors can monitor glucose levels for up to 2 weeks. These platforms, however rely on skin-piercing microneedles, which can cause skin irritation after long-term use or after repeated cycles of application/removal. Biofouling due to cellular response and molecular adsorption is another limitation, particularly with long-term exposure. The substantial cost of each sensor drives the need for week-long operational capabilities. By contrast, since our sweat sensors are completely noninvasive, they do not irritate the skin and their potential to be manufactured at low cost allows for frequent replacement of the disposable microfluidic system, with reuse only of the detachable electronic module. The device minimizes biofouling by isolating the sensors and sample reservoirs from the body via the soft microfluidic system. The multimodal operation (lactate, chloride, pH, and sweat rate) addresses needs beyond those provided by continuous glucose monitoring systems. The results therefore provide a more comprehensive overview of physiological state.

The following presents systematic in vitro studies of each constituent subsystem of these devices, with an emphasis on the wireless, biofuel cell–sensing electronics. Field trials that include (i) continuous monitoring from devices interfaced to the skin for two consecutive days and (ii) collecting data during controlled exercise conditions three times each day, both with correlations to corresponding blood analytes, suggest potential for clinically relevant use of the technology in practical settings.

RESULTS

Hybrid, battery-free, skin-mounted system for sweat sensing

The platform includes two components: a disposable soft, microfluidic network and a reusable, thin NFC electronic module. An exploded view illustration of the overall construction of each of these subsystems is in Fig. 1A. Figure S1 illustrates a cross-sectional schematic illustration of the different layers of the device. A low-modulus (~1 MPa) silicone elastomer, patterned using soft lithographic techniques, defines a set of isolated chambers for colorimetric and electrochemical sensing, a ratcheted channel for quantifying sweat rate and total sweat loss and a collection of interconnecting microchannels with passive, capillary bursting valves (CBVs) for routing sweat through the device. A patterned layer of a skin-compatible adhesive enables robust attachment to the skin, and it defines openings as interfaces between the skin and inlet ports in the bottom side of the microfluidic structure. The soft, flexible construction, as illustrated in Fig. 1B, allows comfortable, water-tight, irritation-free mounting onto curved regions of the body. Figure 1C shows the electronic module, where the NFC interface (~0.1 g) supports both wireless power delivery and data transmission to any NFC-enabled consumer device, such as a smartphone, tablet, or watch. The battery-free design exploits a detachable, bilayer flexible circuit board (diameter, 18 mm; thickness, ~0.5 mm) with a minimal component count for real-time data acquisition from biofuel cell–based lactate and glucose sensors located in the microfluidic structure (diameter, 32 mm; thickness, ~1 mm). Estimates suggest that this platform (~1 g) is nearly 20 times lighter in weight and 4 times smaller in lateral dimension than approaches that rely on battery-powered Bluetooth radios (*20*, *36*, *37*). A previous example of a biofuel cell–based lactate sensor illustrates the underlying sensing principle (*34*). Unlike the system introduced here, this previous work requires a battery-powered Bluetooth low energy module for wireless transmission, with associated significant increases in size and weight. Advantages of the present system include increased comfort and discreet wearability. In addition, the engineered microfluidic structure allows for sweat sample handling with zero cross-talk between the different sensors. The biofuel cell design involves a voltage amplifier with defined sensor element load implemented with a small footprint operational amplifier and miniature passive components. The circuit conditions the signal for digitalization within the integrated NFC chip (TI RF430FRL152H). The analog electronics are robust, with minimal susceptibility to external noise caused by the NFC electronics and fluctuations in the supply voltage.

To enable reuse, the electronics mount onto disposable microfluidic systems with a releasable electromechanical interface. Specifically, a set of thin, small-scale neodymium magnets (diameter, 1 mm; height, 0.5 mm) affixed with conductive adhesives to contact pads of the backside of the electronic platform and another set embedded in recessed wells underneath contact pads of the electrochemical sensors in the microfluidic platform enable reversible, mechanically robust, and self-aligning attachment with low-resistance electrical coupling (Fig. 1D). A net attractive force of ~1.5 N holds the NFC electronics to the disposable patch. Movie S1 demonstrates the robustness of the coupling during vigorous movements. The magnetic attachment is, thus, sufficiently robust for several low to medium intensity physical activities. The device layout can include alternative magnets to enhance the attachment force without significant compromise in the device dimensions. Figure 1E shows a photograph of the complete system. The user first adheres the microfluidic system to the skin and then magnetically mounts the electronics on top. An NFC-enabled portable device or a long-range reader placed in proximity initiates wireless,

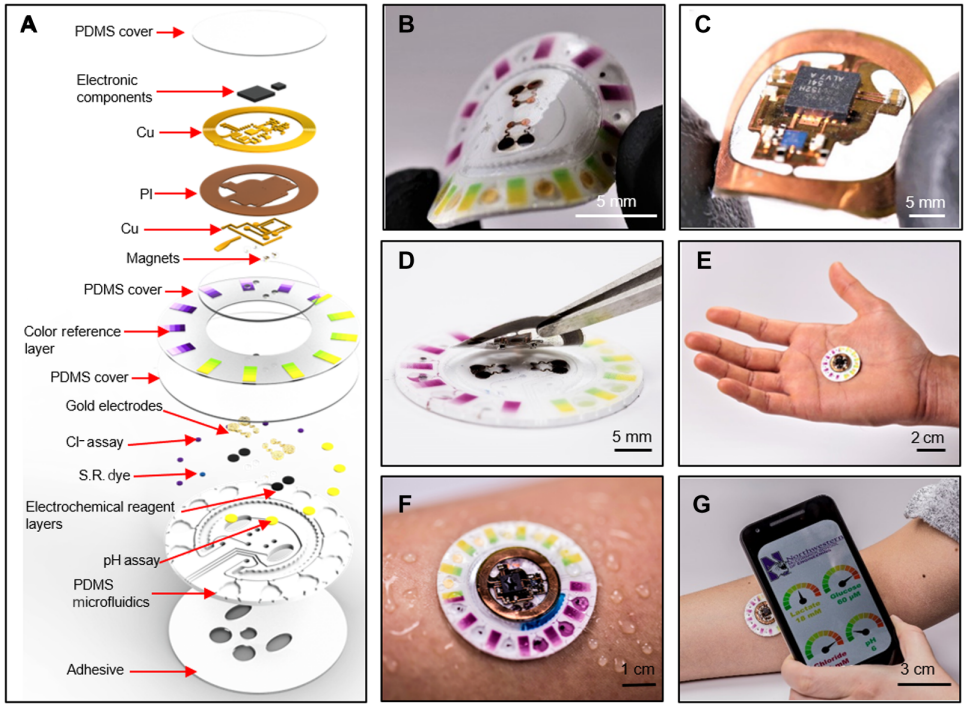

Fig. 1. Device concept. (**A**) Schematic illustrating the exploded view of the complete hybrid battery-free system. PI, polyimide; S.R., sweat rate. Close-up image of (**B**) microfluidic patch with embedded sensors and (**C**) battery-free NFC electronics. (**D**) Image illustrating the reversible magnetic attachment of the NFC electronics to the microfluidic patch. (**E**) Image of the complete system. (**F**) Image illustrating the device during sweating. (**G**) A phone interface that illustrates wireless communication and image acquisition. Photo credit: Philipp Gutruf, Northwestern University.

real-time data acquisition from the biofuel cell–based lactate and glucose sensors. Visual readout or analysis of digital images allows colorimetric quantification of chloride, pH, and sweat rate/loss. Figure 1F shows a system attached to the forearm during sweating. In one example of use, the NFC functionality in a smartphone enables wireless data extraction, and its camera permits acquisition of digital images for colorimetric analysis, as illustrated in Fig. 1G.

Battery-free NFC electronics

The NFC electronics operate in a low-power mode with minimal component count and a small footprint compared to alternative systems. The platform uses a dual-layer, copper-on-polyimide substrate (Pyralux AP8535R, DuPont, Wilmington, DE), laser patterned and populated with a radio frequency (rf) system on a chip that features an integrated microcontroller and a 14-bit analog-to-digital converter with ISO 15693 compatible rf front end. Figure 2A shows a simplified schematic illustration to highlight that amplification relies on a simple voltage follower design with a high-frequency filter that eliminates fluctuations introduced by the electric field of the primary NFC antenna. This NFC electronic subsystem magnetically couples to electrochemical sensors embedded in a disposable microfluidic substrate. Figure 2B shows a completed device adhered to surfaces with small radii of curvature to demonstrate the mechanical robustness of this coupling scheme. Figure 2 (C and D) shows the corresponding current (*I*) versus voltage (*V*) curves associated with the magnetic connection and the variation in phase response for the antenna in response to bending. These results highlight stable antenna performance metrics (i.e., Q factor and resonance peak position) even during mechanical deformations and under cyclical attachment/detachment conditions. Figure 2E shows *I*-*V* curves recorded at regular intervals during repeated cycles of magnetic attachment/detachment. Figure 2F exhibits the effect of bending on the impedance of magnetic contacts over a wide range of frequencies.

Robust operation follows from electrical working principles that tolerate fluctuations in supply voltage during weak NFC coupling to the reader antenna. Because a nonregulated harvesting circuit scheme yields the highest possible efficiency, and therefore the longest operational distance, the analog front end must operate in a manner that is independent of voltage supply to allow for variances in magnetic resonant power transfer and, thus, stable operation in practical scenarios. Using a zero-crossover operational amplifier accomplishes this goal due to the wide operational voltage window that conditions the sensor signal without distortion, regardless of supply voltage. SPICE (Simulation Program with Integrated Circuit Emphasis) software simulation reveals the behavior of the biofuel cell–based lactate and glucose sensors signal conditioning when subject to varying supply voltage (fig. S2). Figure S2 (C and D) confirms stable data acquisition over the entire range of supply voltages. Figure 2 (G and H) shows experimental validation through studies of the effect of distance and angle between three separate devices and a handheld reader with antenna size comparable to a smartphone (5 cm by 3 cm) on sensor signal quality for the case of a constant reference sensor signal (100 mV). In these experiments, a constant current reference signal, applied to the wireless electronics with a 1-megohm load via a constant current source, simulates an electrochemical cell analogous to the glucose sensor configuration. Figure 2G illustrates that the reader records stable signal from the devices at a distance up to ~38 mm. Figure 2H shows the reader's capability for recording uninterrupted, constant signals from the devices at angles up to 70°, with voltage errors of only 2 mV throughout the test, which corresponds to an acceptable variation of ~10 μM for the glucose sensor and ~0.2 mM for the lactate sensor, as described subsequently.

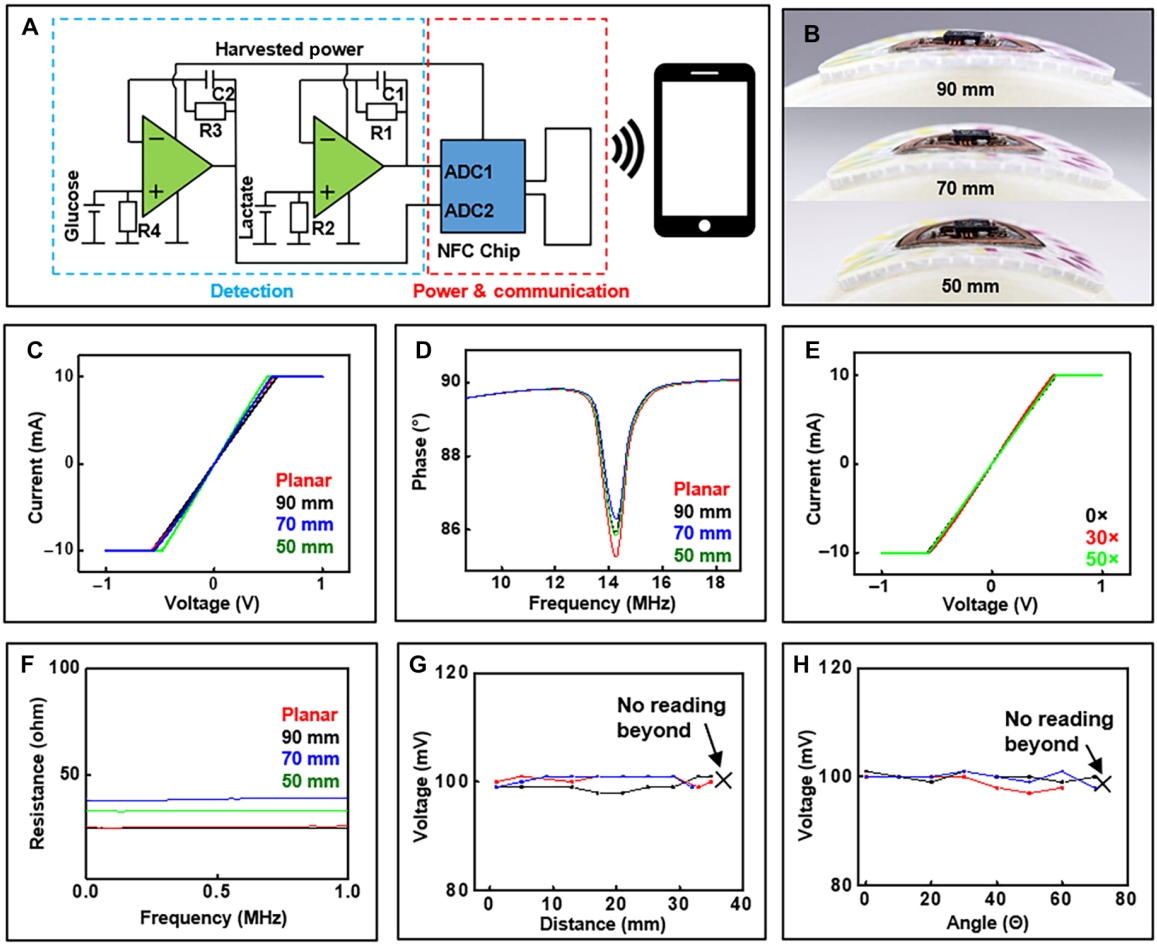

Fig. 2. Electrical characterization of the NFC electronics. (**A**) Simplified schematic illustration of electrochemical sensor readout. ADC, analog-to-digital converter. (**B**) Image illustrating the device bent at decreasing radii. (**C**) *I-V* measurements of shorted sensors recoded with decreasing curvature radii. (**D**) Phase response measurements of NFC electronics with decreasing radii. (**E**) *I-V* measurements of shorted sensors with repeated attachment and detachment of the electronics to the microfluidics. (**F**) Effect of bending on the impedance of magnetic contacts over a wide range of frequencies. Effect of (**G**) distance and (**H**) angle between NFC reader and device on signal recording (n = 3). Photo credit: Philipp Gutruf, Northwestern University.

A distance of ~1 cm is maintained between the device and the reader while studying the effect of orientation between the device and electronics. These results demonstrate the broad range of conditions over which reliable data can be acquired.

Biofuel cell–based electrochemical sensors for lactate and glucose

The biofuel cell design for the sensors is a critical feature of the systems. A scheme that illustrates the components of the lactate sensor is in Fig. 3A, whereby the anode consists of circularly cut carbon nanotube (CNT) paper that provides a conductive, high–surface area substrate to immobilize lactate oxidase enzyme for selectively catalyzing lactate oxidation and the redox mediator tetrathiafulvalene for shuttling electrons between the enzyme's active sites and the underlying CNT paper. According to the datasheet provided by the supplier, the Michaelis constant for lactate oxidase is ~1 mM. The average concentration of lactate in sweat, however, is ~14 mM (*38*). Hence, a diffusion barrier is essential to prevent sensor saturation and to extend the detection limit into the physiological range. Side effects of such a barrier include reduced sensor sensitivity and increased response time. A chitosan and polyvinyl chloride (PVC) membrane coat the anode to minimize leaching of the mediator and enzyme and to extend the linear detection range of the sensor. The cathode consists of a functionalized current collector of gold with an overlayer of platinum black, all coated with a Nafion membrane. The platinum black acts as a catalyst for oxygen reduction, while the Nafion membrane prevents leaching of the platinum black. The fluoride backbone of the Nafion polymer facilitates adsorption of dissolved oxygen onto the cathode's surface, thereby improving the kinetic rate of oxygen reduction. An optical photograph of the complete lactate sensor is in Fig. 3B.

The anodic and cathodic reactions that generate electrical currents in the lactate sensor are proportional to the concentration of lactate. A resistor connected across the sensor transforms the current into a voltage-based signal for detection and wireless transmission via the NFC electronics. The output voltage of the biofuel cell–based sensors increases linearly with increasing load. However, at higher loads, the response time also increases. Hence, the selection of the external loading resistance for the lactate and glucose sensors centers on its ability to generate a voltage signal in the range of 0 to 1 V (measurement range for the NFC chip) for the physiologically relevant concentrations of the two analytes with minimum effect on response time. The response of the sensor with increasing lactate concentration, evaluated in

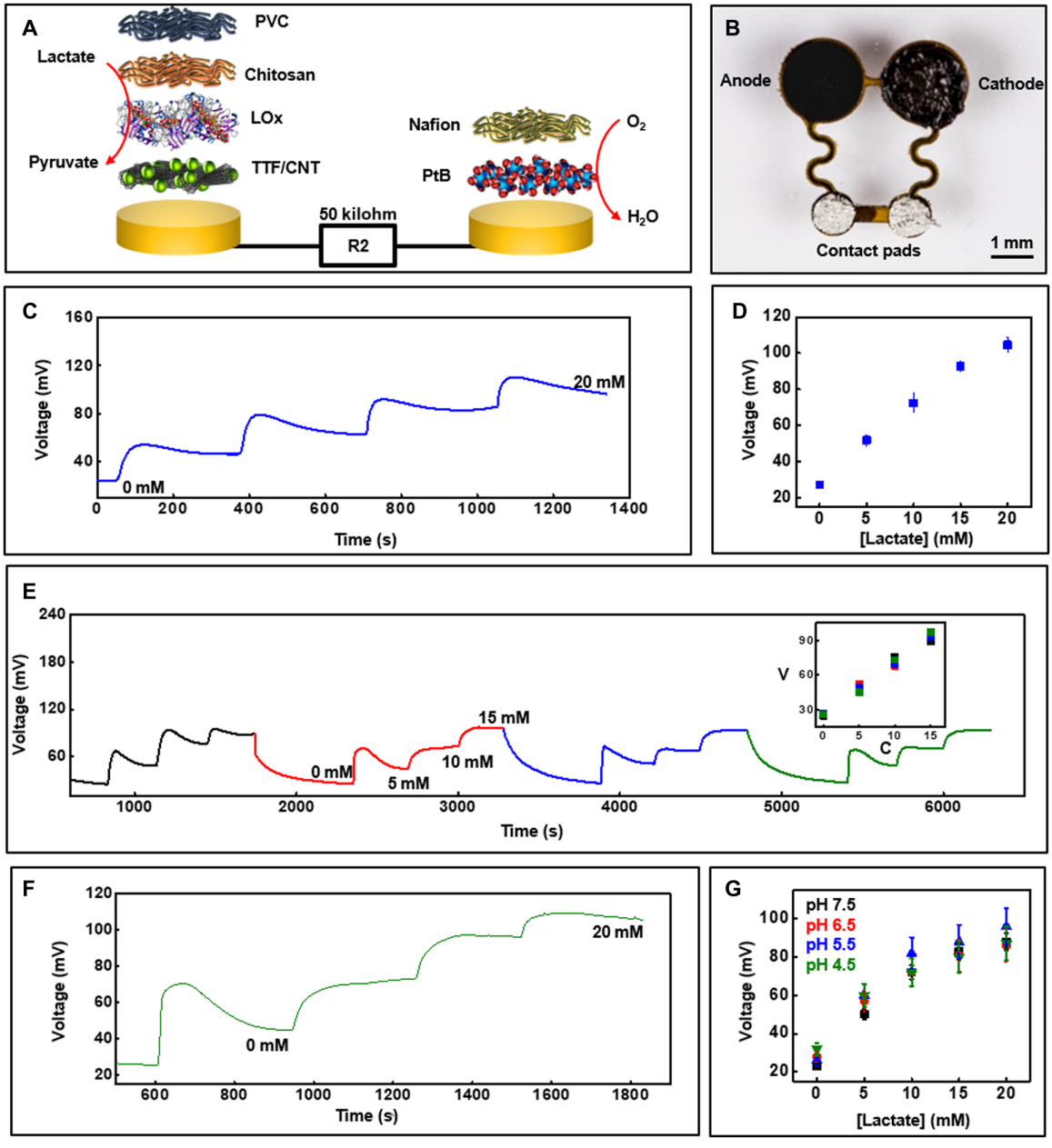

Fig. 3. Lactate sensor characterization. (**A**) Exploded-view schematic illustration of the layer makeup of the biofuel cell–based lactate sensor. LOx, lactate oxidase; TTF, tetrathiafulvalene. (**B**) Image of the lactate sensor. (**C**) Real-time sensor response to increasing lactate concentration in phosphate buffer (pH 7.0) at 25°C and (**D**) the corresponding calibration ($n = 3$). (**E**) Plot illustrating a reversible response for the lactate sensor for four consecutive cycles of varying lactate concentration. Inset shows calibration plot that compares the sensor signal in (E) for the four cycles. V, voltage in millivolts; C, concentration in millimolar. (**F**) Real-time data acquired with increasing lactate concentration in artificial sweat under common physiological sweat conditions [temperature, ~30°C (pH 5.5)]. (**G**) Calibration plot obtained from lactate sensors at ~30°C in artificial sweat with different pH ($n = 3$). Photo credit: Philipp Gutruf, Northwestern University.

phosphate buffer solution under ambient conditions, appears in Fig. 3C (maximum current output, ~2 μA). Figure 3D shows the corresponding calibration plot, which indicates that the sensor signal stabilizes within 300 s and increases linearly with lactate concentration. The spikes and the subsequent signal stabilization follow a typical diffusion-controlled sensor response. This trend is likely due to the presence of PVC and chitosan diffusion barriers. This effect does not represent a major issue in practical applications. The benchtop studies include abrupt increments of the lactate concentration (5 mM steps). In contrast, the sweat analyte concentration varies gradually and on much longer time scales in vivo. This slow temporal variation in sweat analyte concentration allows ample time for the biofuel cell–based sensors to produce a stable response. Figure S3A illustrates the stability of the sensor signal when exposed to 10 mM lactate solution for 20 min, while fig. S3B shows sensor data in the presence of common interferents (ascorbic acid, uric acid, and glucose) in physiologically relevant concentrations. The data illustrate the operational stability of the sensor with negligible effects from interfering chemical species

(~4% increment in signal due to interferents). Some delay in response time for sensors occurs in the presence of the interfering chemicals. However, once stabilized, the signals remain nearly consistent with those exhibited without interfering species. Side reactions such as oxidation of ascorbic acid and uric acid at the Pt-based cathode may explain the observed delays. Figure 3E showcases the reversibility of this response through experiments that involve increasing lactate concentration in a stepwise fashion from 0 to 15 mM, reducing it to 0 mM and then repeating this process for four consecutive cycles. A maximum relative standard deviation (RSD) of ~6% in sensor signal highlights the linear, reversible response to time-varying concentrations of lactate concentrations, with minimal hysteresis (Fig. 3E, inset) across a physiologically relevant range. Figure S3C illustrates an additional reversibility study using a separate lactate sensor for two consecutive cycles (maximum RSD, ~5.5%). Human sweat contains electrolytes, metabolites, and other species (*38*) that could potentially affect the sensor operation. The response in artificial sweat at a representative sweat temperature of 30°C (±3°C) (*39*) with increasing lactate concentration at an average sweat pH of 5.5 (*38*) appears in Fig. 3F. Figure 3G shows calibration plots for lactate sensors in artificial sweat at various physiologically relevant pH values at 30°C (±3°C). The sensitivity of the lactate sensor decreases for concentrations above 15 mM as the pH decreases. The pH-dependent activity of lactate oxidase enzyme likely causes this effect. The calibration plot illustrated in Fig. 3G can be used to compensate the pH effect, based on measurements of pH in the colorimetric region of the microfluidic platform. In addition, fig. S3D shows the lactate sensor response characterized at a higher than usual sweat temperature (37° ± 3°C). The sensors exhibit a maximum SD of 1.1 mV (last 1 min of signal recording) for concentrations up to 20 mM, which corresponds to a maximum error of ~1.3 mM.

A similar approach, applied with a few modifications, yields sensors for glucose. Here, glucose oxidase enzyme is directly dispersed in the Nafion to ensure rapid interaction of glucose with the enzyme and consequent capabilities in detection of micromolar concentrations. The cathode involves a gold-based current collector coated with a suspension of platinized carbon in Nafion solution. Figure 4A illustrates the different components, and Fig. 4B shows an image of the sensor. The voltage signal generated across a biofuel cell–based sensor is proportional to the concentration of the analyte. Hence, a high load (1 megohm) resistor connected across the sensors generates sufficiently high-voltage signals for detecting micromolar concentrations of glucose in human sweat. Comprehensive studies conducted in a manner similar to those for the lactate sensor define the response. Figure 4C summarizes real-time measurements with increasing concentrations of glucose in buffer under ambient conditions, along with a corresponding calibration plot (Fig. 4D; maximum current output, ~0.2 μA). Figure S4 (A and B) illustrates the stability of the sensor signal when exposed to 150 μM glucose solution for 20 min and the effects of common electroactive sweat components (ascorbic acid, uric acid, and lactate) that can potentially affect sensor response. The studies reveal a stable sensor signal with minimal effects of interferents (~12% increment in signal due to interferents). A delayed response to glucose occurs in the presence of interfering chemicals, similar to the case of the lactate sensor, which we also attribute to side reactions occurring at the Pt-based cathode. Figure 4E highlights the reversible nature of the response of the glucose sensor, with a maximum RSD of ~4% for four consecutive cycles of varying concentrations. Real-time data acquired from a similar study using artificial sweat under average physiological sweat conditions (*38*, *39*) [temperature, 30°C (pH 5.5)] appear in Fig. 4F, while Fig. 4G illustrates calibration plots for glucose sensors when exposed to artificial sweat at 30°C (±3°C) at different pH values. The data reveal that pH has a greater effect on the glucose sensor compared to the lactate sensor. A slight decrement of sensitivity in the range of 0 to 100 μM occurs when the artificial sweat pH decreases from 6.5 to 5.5, while the calibration plot shifts upward at pH 4.5. The effect of pH on enzyme activity may contribute to these observations. The calibration plot illustrated in Fig. 4G allows for compensation of this pH effect. Figure S4C shows the glucose sensor response characterized at a higher than usual sweat temperature (37° ± 3°C).

Separately, fig. S5 illustrates effect of bending stress on the device. Applying the device on a curved surface (radius, 25 mm) and measuring lactate and glucose sensor response reveal negligible effects on sensor performance. This behavior can be attributed to the thin, flexible nature of the sensors and to the serpentine interconnects designed to accommodate mechanical strains. Table S1 compares limit of detection (LOD) and sensitivity of the present device with that of previously published systems. LOD is calculated as $3 \times S_b/S$, where S_b is the SE of the baseline response and S is the slope of the calibration curve. Values reported in the table from previously published work represent estimates since most papers do not report the LOD or sensitivity. LOD calculations for these devices use the linear regression method. Furthermore, earlier demonstrations rely on amperometric techniques and, hence, have sensitivities in μA mM^{-1} cm^{-2}, while the present biofuel cell–based sensors have sensitivities with units of mV mM^{-1} cm^{-2}.

Colorimetric assays and microfluidics

The disposable microfluidic substrate houses the electrochemical sensors and various colorimetric assays, and it supports valves, channels, and reservoirs for handling small volumes of sweat delivered into the system by the action of the glands themselves. The designs and the chemistries rely on recently reported results (*21*, *40*).

For chloride concentration, the colorimetric assay relies on silver chloranilate, a chemical that complexes with chloride ions to generate a species with a distinct purple color (*41*). Mixing silver chloranilate with polyhydroxyethylmethacrylate solution creates a gel-like suspension that immobilizes the insoluble silver by-product in the assay well. The result prevents migration of silver particulates during flow of sweat in the microfluidic channel, thereby eliminating their effects on color extraction. The extent of change in lightness "L," a hue-independent parameter from the Lab color space analysis, determines the concentration of chloride through a linear calibration curve, as shown in Fig. 5A (*42*). This chemical reaction provides a more reliable, accurate colorimetric response compared to previously reported alternatives for analysis of chloride in sweat (*21*, *43*). Similarly, paper pads coated with a pH-sensitive dye and a phase-transfer catalyst serve as a colorimetric means for determining pH. The evolution of color as a function of pH over a physiologically relevant range is in Fig. 5B. Calibration plots reveal the linear relationship between the *R* values (of the RGB code) at different pH levels. Simple color reference bars developed for each of these calibration plots facilitate visual or digital color extraction and conversion to concentration. The colorimetric assays exhibit high reproducibility (maximum RSD, ~2.6%).

Color analysis software allows for extraction of color values from the assay chambers and color reference markers for estimating the concentration of chloride and pH of sweat (fig. S6 and Materials and Methods). Studies conducted under various lighting conditions highlight the accuracy of the data acquisition process (fig. S7, A to D). Such robustness can

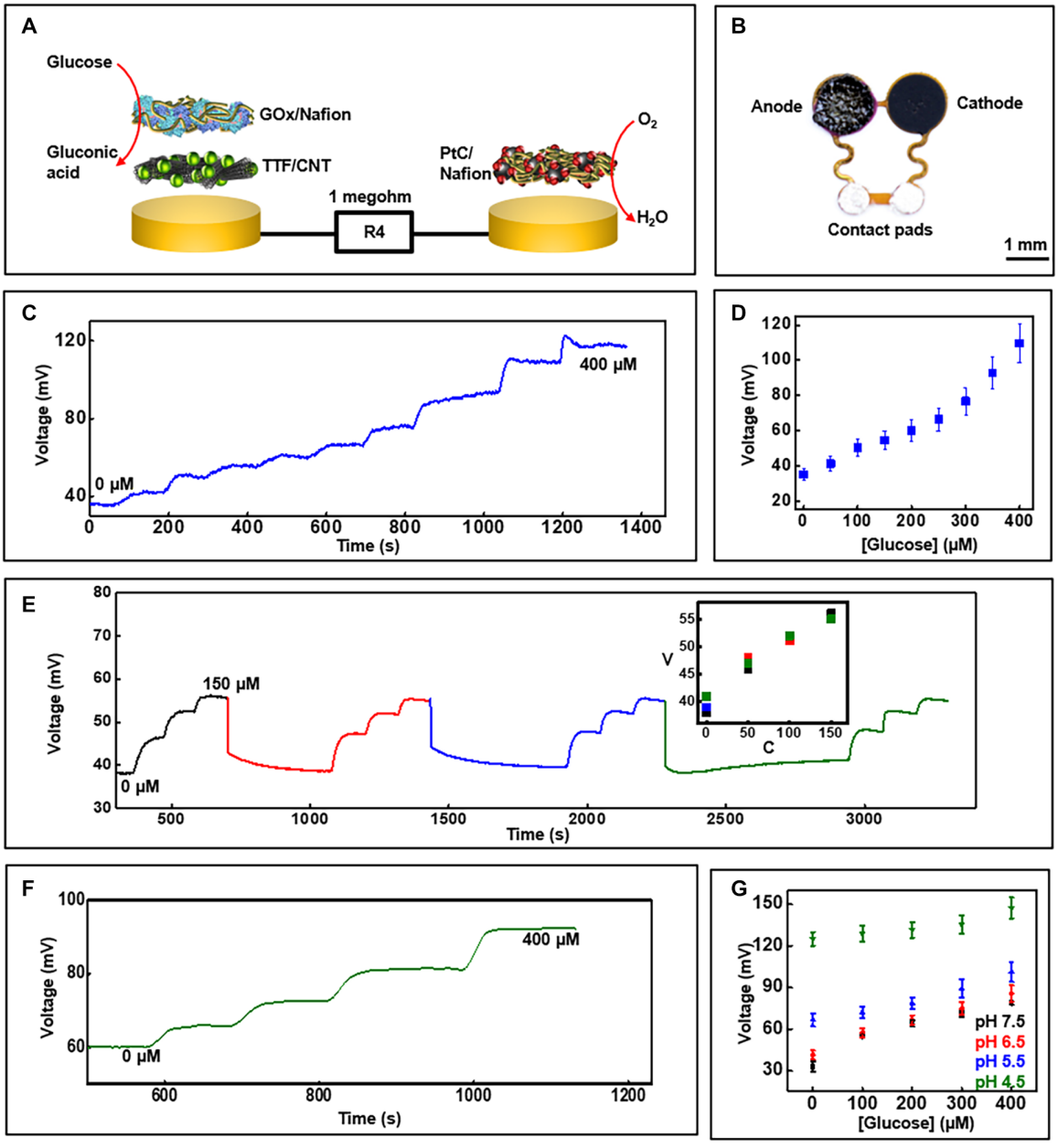

Fig. 4. Glucose sensor characterization. (**A**) Exploded-view schematic illustration of the layer makeup of the biofuel cell–based glucose sensor. GOx, glucose oxidase; PtC, platinized carbon. (**B**) Image of the glucose sensor. (**C**) Real-time sensor response to increasing glucose concentration in phosphate buffer (pH 7.0) at 25°C and (**D**) the corresponding calibration (n = 3). (**E**) Plot illustrating the reversible response of the glucose sensor for four consecutive cycles of varying glucose concentration. V, voltage in millivolts; C, concentration in micromolar. Inset shows calibration plot comparing the sensor signal plotted in (E) for the four cycles. (**F**) Real-time data acquired with increasing glucose concentration in artificial sweat under common physiological sweat conditions [temperature, ~30°C (pH 5.5)]. (**G**) Calibration plot obtained from glucose sensors at ~30°C in artificial sweat with different pH (n = 3). Photo credit: Philipp Gutruf, Northwestern University.

be attributed to the use of color reference bars for calculating analyte concentration (details for color analysis appear in Materials and Methods). Stability studies reveal that assay colors remain stable for at least 2 days when stored under humid conditions to minimize solution evaporation and concomitant variation in analyte concentration (fig. S7, E to H).

The part of the system designed to measure sweat rate/loss involves a simple, circular channel with a water-soluble dye located near the inlet (Fig. 5C). The incoming sweat dissolves the dye as it flows past, thereby creating a visible, colored fluid with an easily identifiable filling front in the channel (*44*). The position of this front defines the local rate and loss of sweat from the corresponding location on the skin. Although the local sweat rate depends on mounting location, for a given location, this locally measured sweat loss can be quantitatively correlated to the total body sweat loss (*21*, *39*). The sensor reported here is calibrated to total loss when used on the forearms. Application of these devices to other regions of the body requires recalibration. The presence of the device may locally alter the sweat rate. However, optimization of the sweat

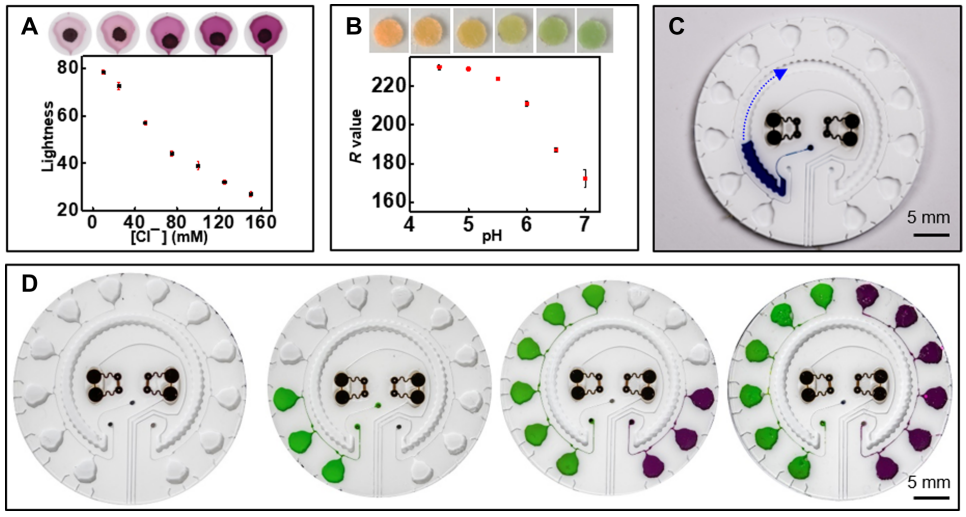

Fig. 5. Colorimetric assay characterization. Calibration and corresponding color evolution for physiologically relevant levels of (**A**) chloride (n = 3) and (**B**) pH (n = 3). (**C**) Filling of sweat rate sensor. The arrow indications the direction of filling. (**D**) Image illustrating the chrono-sampling feature of the microfluidic system. Photo credit: Jungil Choi and Jonathan Reeder, Northwestern University.

collection regions defined by the patterned adhesive layer minimizes the effects of local compensatory sweating (*39*). Figure S7I shows a linear correlation between data acquired from the sweat rate sensor to the normalized total, or full-body, sweat loss. The sweat collection volume from the microfluidic channel yields estimates of the total body sweat loss with a maximum error of ~23%. The total sweat loss is calculated by measuring the difference in body weight before and after the workout, with no consumption of water during the test. In this particular design, the channel volume (~58 μl) and the dimensions of the inlet interface to the skin allow tracking of sweat loss for up to 6 hours based on an average sweat rate in the range of 12 to 120 μl/hour per cm^2 (*21*).

Although these assays have an irreversible response, time-dependent changes in sweat composition can be captured by using fluidic designs that enable time-sequential sampling (chrono-sampling) of sweat using passive valve constructs (*40*, *45*). The example in fig. S8A uses collections of CBVs to enable sequential filling of a series of independent microreservoirs, each pre-impregnated with a colorimetric reagent. Briefly, CBV #1 has the smallest bursting pressure (BP) due to its wide channel width (200 μm) and small diverging outlet angle (21°). CBV #2 has the second smallest BP due to its larger diverging angle (90°) with a width that is the same as that of CBV #1. When sweat encounters the intersection between CBV #1 and CBV #2, it flows through CBV #1 due to its smaller BP. After filling the chamber, the sweat flows to CBV #2 because CBV #3 has the highest BP due to its small width (50 μm). The sweat gland generates fluidic pressure through osmotic effects associated with the concentration difference between sweat and plasma. The microfluidic platform contains CBVs specially designed to open within the physiological range of sweat pressures. Hence, the pressure generated by the glands themselves is sufficient to open each chamber (*39*, *45*). Using this process, the device collects and stores sweat in time sequence in separate chambers. The left and right sides of the device provide chrono-sampling analysis of pH and chloride, respectively.

Since the electrochemical sensors for lactate and glucose are reversible, a single-chamber design with a single channel to divert sweat from this chamber to an outlet is sufficient. These two microfluidic structures flank either side of the patch. The sweat sensor channel resides in between the regions for electrochemical and colorimetric sensing. Figure S8B and Fig. 5D highlight the multimodal microfluidic substrate and chrono-sampling features of the system. Circular holes (diameter, 1 mm) serve as inlets in the base of the microfluidic platform for the sweat rate, chloride, and pH sensors, while ellipsoidal-shaped holes (major axis, 5 mm; minor axis, 3 mm) act as inlets for glucose and lactate sensors. The skin-adhesive layer has corresponding circular (diameter, 3 mm) and ellipsoidal (major axis, 6 mm; minor axis, 4 mm) openings.

Human trials

Field testing involves healthy, nondiabetic, consenting human volunteers (three males) instrumented with devices on the upper wrist. Thorough cleaning of the skin with alcohol wipes helps minimize erratic data due to residual skin contaminants while improving the adhesion of the device to the skin. Studies follow guidelines laid down by the Institutional Review Board, Northwestern University. The physical exercise involves cycling on a stationary bike with increasing resistance. Real-time data acquisition during each trial occurs either through a compact, short-range reader or an extended, long-range reader that was positioned in the vicinity of the device. As illustrated in Fig. 2 (G and H) and fig. S2, the long-range reader offers significant spatial latitude to the user during data collection. Advancements in rf technology for various indoor (*46*) and smart city (*47*) applications promise continued increases in the prevalence of long-distance readers. These readers can be installed in indoor fitness centers or medical/rehabilitation facilities for continuous acquisition of data from these biofuel cell–based lactate and glucose electrochemical sensors. Figure 6A shows an image of a subject on a stationary bike wearing the device, with an extended antenna (60 cm by 30 cm) in the background. Figure 6B summarizes the effective communication distance between the device and the antenna (shown in Fig. 6A); presented here is the largest distance that enables successful operation. The data show a maximum operating distance of ~18 cm with this configuration.

Figure 6 (C to H) shows a device after cycling, along with a summary of data acquired from the lactate and glucose sensors for subjects #1 and #2, respectively. For both subjects, the respective sensors produce voltage signals that yield corresponding concentrations based on calibration

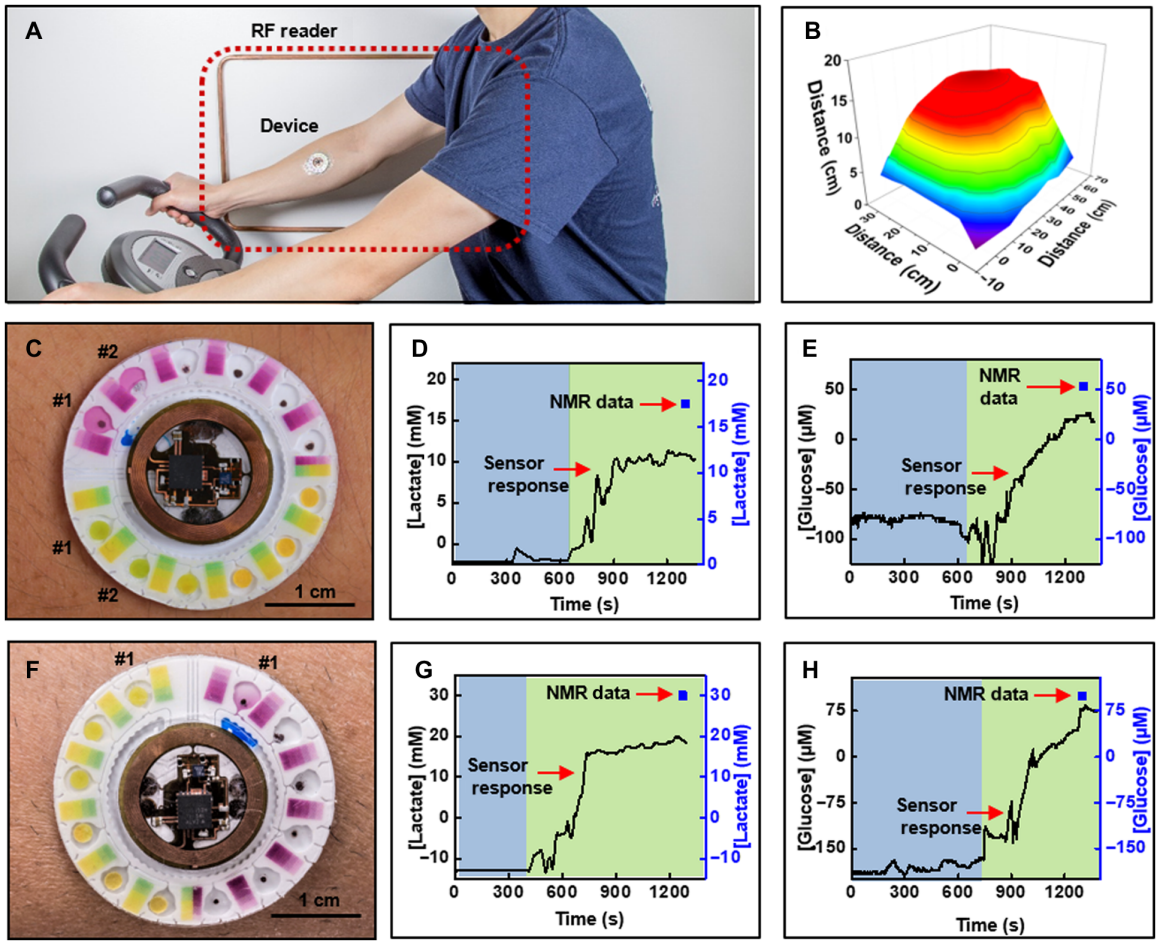

Fig. 6. Human trials. (**A**) Photograph of a subject wearing a wireless battery-free hybrid sensor system. (**B**) Reading distance with a large NFC antenna. (**C**) Image of complete system captured after a bout of cycling by subject #1. Real-time wirelessly acquired sweat concentration levels for (**D**) lactate and (**E**) glucose, respectively. (**F**) Image of complete system captured after a bout of cycling by subject #2. Real-time wirelessly acquired sweat concentration levels for (**G**) lactate and (**H**) glucose, respectively. (D, E, G, and H) Blue and green regions represent conditions before and after collection of sweat, respectively. Photo credit: Philipp Gutruf, Northwestern University.

plots obtained at ~30°C (usual sweat temperature) (*39*). Analyte concentrations reported in these studies are consistent with previously published studies (*12*, *20*) and with average concentration values in sweat [14 mM lactate, 170 μM glucose, 23 mM chloride (pH 5.5)] (*38*). Image analysis of Fig. 6 (C and F) reveals that the concentration of chloride is 62 ± 5 mM (subject #1; chamber #1), 36 ± 5 mM (subject #1; chamber #2), and 34 ± 2 mM (subject #1; chamber #1); the pH is 6.3 ± 0.05 (subject #1; chamber #1), 6.2 ± 0.03 (subject #1; chamber #2), and 6.4 ± 0.1 (subject #2; chamber #1); and the sweat rate is ~0.52 μl/min (subject #1) and ~0.88 μl/min (subject #2). Separate analyses using conventional techniques such as commercial benchtop chloridometry, pH analysis, and high-resolution nuclear magnetic resonance (NMR) spectroscopy provide points of comparison. These methods are widely used analytical chemistry approaches in sweat studies (*48*, *49*). Figure S8C illustrates a typical NMR spectrum. Table S2 summarizes the results. In all cases, measurements from the device correlate well with those using conventional techniques. The data reveal that NMR measurements, however, consistently overestimate the sweat glucose and lactate values by approximately a factor of 2 when compared to corresponding data acquired from the device. The differences could arise from a combined effect of comparing real-time data acquired from our sensor to time and spatially averaged sample concentration measured by NMR and partial evaporation of sweat during collection and changes in measured concentrations due to steps involved in lyophilization and redistribution of the solute in deuterium oxide for NMR analysis. The sample collection and analysis for conventional methods are independent of the sensor application and subsequent data acquisition. Another set of human trials (six males and two females; age, 18 to 45 years) involves analysis of chloride and performing a cycling session (15 to 20 min) while simultaneously collecting sweat samples for high-performance liquid chromatography (HPLC) analysis. Figure S9 shows a linear correlation between the data acquired from the colorimetric chloride assay with the sweat chloride concentrations acquired from HPLC, thus illustrating good performance of the colorimetric chloride assay for sweat analysis.

Figure 7A and fig. S10 illustrate additional functionality of the device for potential long-term monitoring of sweat glucose and lactate levels over multiple days. The irreversible nature of the colorimetric assays limits them to a single-use mode, as the reagents cannot be recovered after reacting with sweat chloride and hydronium ion. The concentration range of sweat glucose varies among individuals and fluctuates depending on the blood glucose level. The blood glucose and, subsequently, sweat glucose concentration increases after consumption of food and then gradually stabilizes. Similarly, a previous report

suggests correlation between sweat lactate and corresponding blood levels (*22*). The human trails aim to study these concentration fluctuations in blood and sweat and to explore possible correlations between the two. In the first set of studies, the subjects wear the device for two consecutive days and, on each day, execute a cycling exercise (15 to 20 min) in the morning in fasting state, followed by another cycling bout 20 min after consuming 150 g of sweetened drink and then again 2 hours after lunch in the evening. Separate measurements using commercial blood lactate (Lactate Plus; Nova Biomedical, MA) and blood glucose (Accu-Chek Nano Blood Glucose Meter, Roche Diabetes Care Inc.) meters capture blood lactate and glucose levels before and after each cycling bout, as points of comparison.

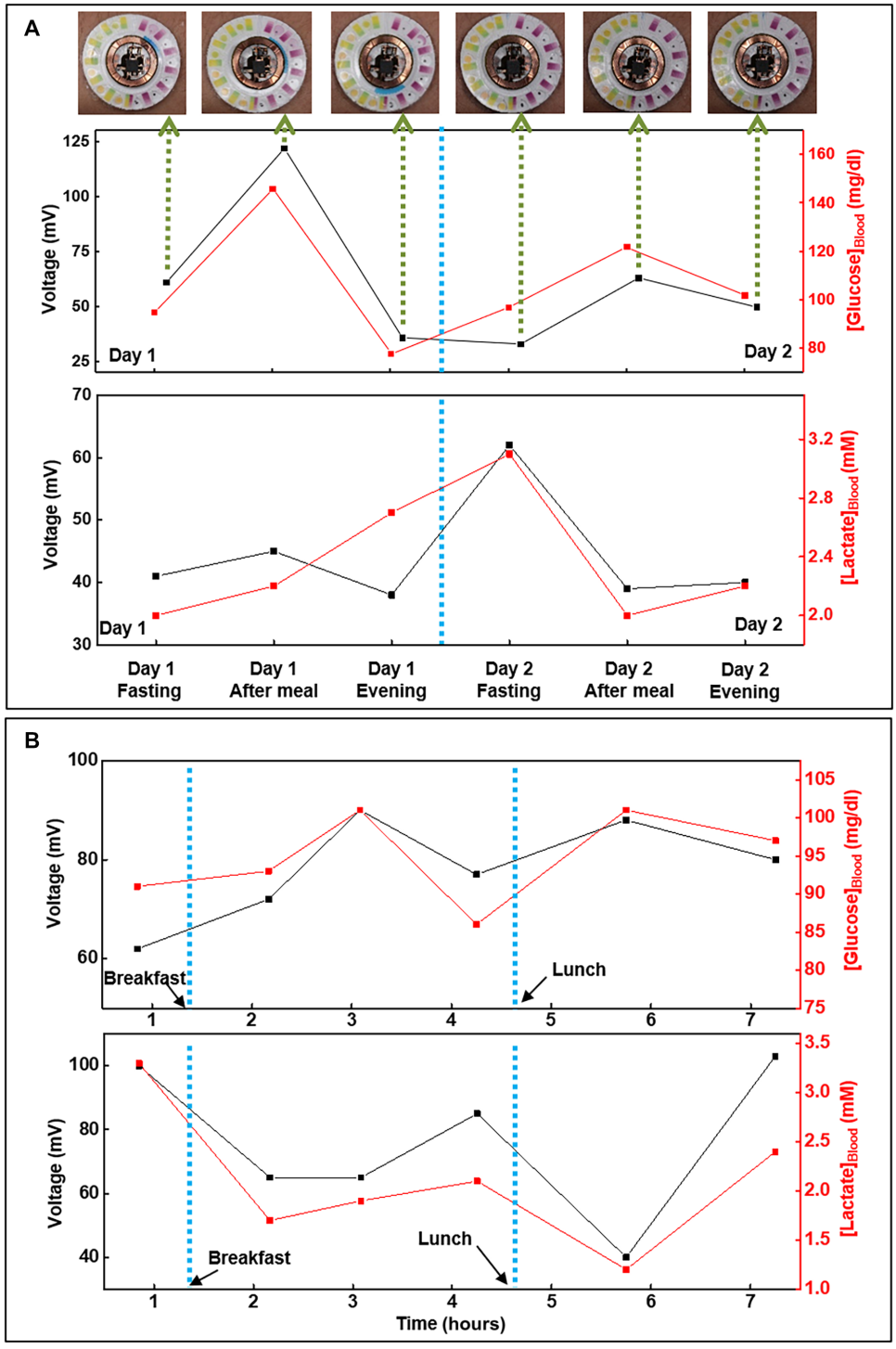

Fig. 7. Human trails. Correlation of data acquired from biofuel cell–based glucose and lactate sweat sensors with that acquired from blood glucose and lactate meters, respectively, over a period of (**A**) 2 days and (**B**) 1 day for subject #1 (with time lag compensation). Photo credit: Philipp Gutruf, Northwestern University.

The second set of studies focuses on comparing temporal variations in glucose and lactate levels in blood and sweat due to consumption of food and engagement in physical exercise. Here, the subjects wear the device over the course of a day and perform a series of periodic exercise sessions (15 to 20 min) on a stationary bike. The subjects begin the study in a fasting state and cycle 30 min before and 30 and 90 min after consuming breakfast and lunch. Blood tests use protocols similar to those for the first set of studies. Figure 7 (A and B) shows data acquired for subject #1 during these long-term sweat monitoring studies, while figs. S10 and S11 illustrate data for additional subjects. Photographs of the device at different stages of the study, as shown in Fig. 7A and fig. S10, indicate robust adhesion to the skin throughout. Analysis reveals that the blood glucose and lactate levels after each session follow trends that are qualitatively similar to those of data measured in sweat using the skin-interfaced devices. The sweat glucose values lag behind those acquired from blood tests by ~30 to 60 min, while a much smaller time lag exists between blood lactate and sweat lactate. Similar time lags appear in studies of various noninvasive (*26*) and minimally invasive (*50*) chemical sensors and can be attributed to the complex biological pathways through which blood constituents reach other biofluids. Analysis of the human trial data reported in Fig. 7B and fig. S11 at specific time points yields correlations between corresponding analyte concentrations in sweat and in blood. The comparison involves blood values for glucose and lactate just before and after each 15- to 20-min cycling session, respectively (fig. S12). The data reveal a relationship between concentrations of these two metabolites in sweat and blood. The results suggest some potential for using sweat sensors as a noninvasive means for tracking blood glucose and lactate concentrations. Error bars for the data from the sweat sensors represent the SDs for the last 1 min of data recording (maximum SD of 2.5 and 3.9 mV for lactate and glucose sensors, respectively). Error bars for the blood meters correspond to data provided by the respective vendors (RSD of 5% and SD of 0.12 mM for glucose and lactate strips, respectively). Contamination caused by residual analytes from previous sweating sessions may explain the outliers (marked in red circles). Modifying the microfluidic designs to optimize fluid flow and purging in the reaction chambers is a potential strategy to eliminate these outliers. In addition, replacing the microfluidics more frequently remains a reliable and viable solution due to the convenient detachability and low-cost nature of the microfluidic component.

These findings are generally in agreement with those of previous studies that compare lactate and glucose levels in blood to those measured in sweat using conventional collection and ex situ analysis techniques (*22*, *25*, *26*). Further support for the long-term stability of the sensors follows from comparisons of signals produced by a pair of devices after the 2-day trial with an unused pair (fig. S13, A and B). The data show that the performance of the glucose sensor diminishes minimally, while the response of the lactate sensor decreases by ~20% even after these rigorous 2-day trials. These results represent the first examples of long-term use of skin-interfaced sweat sensors. An initial transient behavior at the beginning of the used glucose sensor is observed, which may be attributed to the stabilization of the sensor signal when exposed to a different solution (buffer) after being exposed to human sweat for 2 days. In any case, this should not be a matter of concern as the signal stabilizes within 10 to 20 s.

A 2-day trial with a human subject enables comparisons of the response of biofuel cell–based glucose and lactate sensors (n =3 for each analyte) to measurements by NMR. The study involves applying the sensors (right forearm) and leaving them in place for two consecutive days, with 15- to 20-min cycling sessions twice on each day. Simultaneously for each session, we collected sweat samples from the other forearm (left) for NMR analysis, using absorbent pads. Figure S13 (C and D) summarizes the results. The data reveal quantitative agreement between the data from our wearable sensors and NMR analysis to within experimental measurement uncertainties and expected variations between sweat collected from the right and left arms. Additional analysis of the data indicates that the glucose and lactate sensors show a maximum RSD of ~16 and ~10%, respectively. By comparison, commercial blood glucose meters (Accu-Chek Nano Blood Glucose Meter, Roche Diabetes Care Inc.) have RSD of ~10% (for ~85% of test strips). The uncertainty reported for NMR data represents the SD for NMR analysis of sweat samples in triplicates. The comparatively large uncertainties for glucose follow from its relatively low concentration in sweat. Over the course of these 2-day experiments, the glucose sensor response remains constant, while lactate sensor signal decreases by ~20%. These observations are consistent with data illustrated in fig. S13 (A and B).

Additional long-term studies of the stability of both glucose and lactate sensors (n = 3) under conditions experienced during wearable applications, but performed on the benchtop, remove any possible variabilities associated with a human interface. Figure S13 (E and F) illustrates the results. Simulation of wearable conditions involves wrapping the devices around a 35-mm-radius cylinder and testing with artificial sweat at 30° ± 3°C. We rinsed the sensors with buffer and stored them under ambient conditions while wrapped over the cylinder, when not in use. The data reveal stable sensor response throughout the first 6 days (maximum RSD of 1.9 and 4.4% for glucose and lactate sensors, respectively) and a ~13 and ~23% signal decrement for glucose and lactate sensors, respectively, by 8 days. These studies and the on-body data in fig. S13 (A to D) suggest that the modest drifts in the response of the lactate sensor in 2-day human subject trails may result from biofouling, due to the comparatively low resiliency of the lactate oxidase enzyme.

Although these data highlight the promise of this technology, widespread use, commercialization, and implementation will require further platform characterization and optimization. For example, further refinement of the enzyme immobilization techniques and the use of enzyme stabilizers (*51*) may be needed to enhance the long-term storage and operational stability of these sensors. Another limitation is that the battery-free device provides data from the electrochemical sensors only when a reader is present in its vicinity. Future work will be needed to allow for wireless sensing platforms that offer continuous logging of data generated by the sensors even in the absence of a reader near the device. In addition, although the sweat lactate and glucose concentrations follow dynamics similar to those obtained from blood tests, with a certain time lag, the results show person-to-person variability. This variability may follow from the complex biological pathways through which concentrations of the biomarkers in blood translate to those in sweat and the dependency of these pathways on subject-specific factors such as metabolic activity, insulin sensitivity, and fitness level. Further studies may indicate that calibrations against corresponding blood values can account for this variability among users and thereby provide meaningful results for quantities such as the concentrations of glucose and lactate. Commercial continuous glucose monitoring systems use this technique. Such evaluations require large population studies of subjects engaged in various physical activities. These studies represent topics of future work.

DISCUSSION

The electronic designs, integration methods, and materials reported here serve as the foundations for light-weight, miniaturized, soft, battery-free, skin-interfaced technologies that combine biofuel cell sensors, colorimetric assays, NFC electronics, and soft microfluidics for simultaneous detection of lactate, glucose, chloride, pH, and sweat rate/loss. Together, these parameters provide a greater depth of understanding about physiological state under various physical stressors than that possible by monitoring a single parameter. The result is a wearable chemical sensing platform that is much lighter, smaller, and cheaper than the earlier reported wearable sensors with similar performance capabilities. A releasable magnetic coupling scheme for joining the microelectronic and microfluidic subsystems allows for reuse of the former and for single-use operation of the latter. The wireless interface enables both battery-free operation and robust acquisition of digital data generated by the biofuel cell–based electrochemical sensors. Human subject studies demonstrate that these devices can attach robustly to the soft, curved surfaces of the skin without failure during physical exercise, thereby providing continuous, multimodal information associated with sweat loss and sweat chemistry, both of which can be used to assess physiological health, performance, and fatigue. Rigorous 2-day field studies and correlation of data acquired by glucose and lactate sweat sensors with blood levels demonstrate both the ability for long-term use and the potential for noninvasive tracking of blood analyte concentrations. Future efforts will focus on further optimizing device performance and validating its use in extensive large-scale human trails including diabetic patients. Adapting the designs and materials introduced here for applications in tracking patients with kidney disease, in screening for cystic fibrosis, in monitoring pharmacokinetics, and in measuring effects of pressure ischemia and stress markers represents promising directions for future research.

MATERIALS AND METHODS

Fabrication of the microfluidic module

The fabrication process began with sequential cleaning of a 4″ silicon wafer with isopropyl alcohol, acetone, deionized water and a final rinse with isopropyl alcohol. Next, spin coating a 15-μm-thick film of photoresist (KMPR 1010; MicroChem, MA, USA) followed by baking at 110°C for 5 min on a hot plate prepares the system for photolithographic patterning to define the geometry of the microfluidics. Exposing the wafer to ultraviolet (UV) light through a photomask mounted on the wafer followed by baking at 110°C for 3 min in a closed chamber and then for 2 min in an open setup patterned the photoresist. Immersing the substrate in developer solution (AZ 917 MIF; Integrated Micro Materials, TX, USA) completed the process. Subsequently, deep reactive ion etching (STS Pegasus ICP-DRIE, SPTS Technologies Ltd.) created 600-μm-deep micropatterned trenches in the silicon wafer. Last, spin coating poly(methyl methacrylate) (PMMA; MicroChem, MA, USA) on the pattered silicon mold and baking at 180°C for 3 min primed the mold to facilitate release of polydimethylsiloxane (PDMS; SYLGARD 184, Dow Corning, MI, USA) cast and cured on top, as described next.

Dispersing 5 weight % (wt %) white silicone (Reynolds Advanced Materials, IL, USA) into a transparent PDMS precursor (10:1; SYLGARD 184) yielded a thick liquid cast onto the mold by spin coating at 200 rpm. Curing at 70°C for 1 hour yielded a 700-μm-thick, soft, white microfluidic structure. A mechanical punch tool defined 1-mm-diameter inlet holes for the colorimetric channels and ellipsoidal inlet holes for the electrochemical chambers. Pouring PDMS (10:1) on a PMMA-coated silicon wafer, then spin-casting at 400 rpm, and curing at 70°C for 1 hour produced a uniform, 200-μm-thick slab as a cap for the microfluidic platform. An additional layer of PDMS (60:1) spin-casted at 1000 rpm and cured for another 1 hour at 70°C formed a thin, tacky coating. Separately, a commercial laser printer (Konica Minolta C454 PS Color, Tokyo, Japan) printed color reference markers on a 25-μm-thick polyester (PET) film (FLX000464; FLEXcon, MA, USA), and a CO_2 laser (Universal Laser Systems, AZ, USA) defined sweat inlet holes in a skin-adhesive membrane (PC2723U, Scapa Healthcare). Assembly of the microfluidic patch involved placing the colorimetric assays, electrochemical sensors, and neodymium magnets (D0105 Nickel; SuperMagnetMan, AL, USA) into their respective chambers and then laminating the sticky side of the capping layer onto the top of the microfluidic patch. Plasma treating a skin-adhesive membrane, the color reference marker film, and the microfluidic platform with a handheld corona generator yielded hydrophilic surfaces that allowed efficient bonding of the stack to complete the fabrication.

Development of colorimetric assays for chloride and pH

The colorimetric chloride assay solution consisted of 50 mg of silver chloranilate (MP Biomedicals, CA, USA) dispersed in 200 μl of 2 wt % polyhydroxyethylmethacrylate (Sigma-Aldrich, MO, USA) methanolic suspension. Drop-casting 0.5 μl delivered this chloride assay cocktail in the chambers designated for chloride sensing. Suspending 4 ml of universal pH dye (Thermo Fisher Scientific, NH, USA), 274 mg of PVC (molecular weight, ~233,000; Sigma-Aldrich, MO, USA), 635 μl of *o*-nitrophenyloctylether (Sigma-Aldrich, MO, USA), and 508 μl of Aliquat 336 (Sigma-Aldrich, MO, USA) in 10 ml of tetrahydrofuran (Sigma-Aldrich, MO, USA) yielded the pH assay solution. Dip-coating filter papers (Sigma-Aldrich, MO, USA) in the pH cocktail for 10 s and allowing them to dry under ambient conditions for 15 min formed the solid-state pH assay. Cutting the pH assay paper into circular pads using a metal punch (diameter, 2 mm) and placing them in each of the chambers designated for pH sensing completed the process.

Fabrication of biofuel cell–based electrochemical sensors for lactate and glucose

Electron beam evaporation (AJA International Inc., MA, USA) formed a thin film of chromium (thickness, 10 nm) as an adhesion layer, followed by a layer of gold (thickness, 100 nm) as a conductor on a 75-μm-thick sheet of polyimide (Argon Inc., CA, USA). A UV laser (LPKF, Germany) patterned the gold-coated polyimide sheet to define the circular current collector, serpentine interconnects, and contact pads. The first step in realizing a biofuel cell–based lactate sensor involved punching out circular pads (diameter, 2 mm) of CNT paper (Buckypaper, GSM 20; NanoTechLabs, NC, USA). Coating with 2 μl of 0.1 M tetrathiafulvalene (Sigma-Aldrich, MO, USA) solution prepared in acetone/ethanol (1:9, v/v) and 4 μl of lactate oxidase (Toyobo Chemicals, Japan), and allowing them to dry, yielded enzyme-functionalized CNT pads. The enzyme solution resulted from dispersing the enzyme (60 mg/ml) in 0.1 M phosphate buffer containing 0.25 wt % glutaraldehyde (Sigma-Aldrich, MO, USA). Subsequently, drop-casting and drying 2 μl of chitosan [Chemical Abstracts Service (CAS) number 9012-76-4; Sigma-Aldrich, MO, USA] suspension prepared in 0.1 M acetic acid onto each pad formed a chitosan-based membrane. Dipping the dried pads into the chitosan solution for 5 s and then allowing them to dry resulted in an additional chitosan membrane. Last, dipping the pads for 5 s in 3 wt % PVC (CAS number 9002-86-2; Sigma-Aldrich,

MO, USA) suspension in tetrahydrofuran and thoroughly air drying them formed the outer layer of PVC membrane. Conductive silver glue then bonded the pads to the gold current collectors to complete the anode functionalization process. The cathode for the lactate sensor resulted from drop-casting 15 µl of platinum black (10 mg/ml; Sigma-Aldrich, MO, USA) suspension prepared in deionized water, followed by applying 1 µl of Nafion 117 solution (Sigma-Aldrich, MO, USA), onto the cathode designated gold current collector. Storing the sensors at 4°C for at least 1 week before use allowed the chitosan and PVC membranes to stabilize. Fabrication of biofuel cell–based glucose sensors involved steps similar to those discussed for the lactate sensor with some modifications. The process began with drop-casting 1 µl of 0.1 M tetrathiafulvalene solution onto CNT pads. Separately, preparing a solution (40 mg/ml) of glucose oxidase in 0.1 M phosphate buffer containing bovine serum albumin (10 mg/ml; Sigma-Aldrich, MO, USA) and a 1 wt % suspension of Nafion in 0.1 M phosphate buffer and then mixing of the two suspensions in equal volumes yielded the enzyme-coating suspension. Application of 2 µl of the enzyme-coating suspension functionalized the tetrathiafulvalene-coated CNT pads. Conductive silver glue bonded the pads to the gold current collectors to complete the anode. The glucose sensor cathode resulted from preparing a suspension (10 mg/ml) of 10% platinum on carbon (Sigma-Aldrich, MO, USA) in a 2 wt % ethanolic suspension of Nafion, followed by casting 5 µl of the suspension on each current collector. Storing the sensors at 4°C for at least 1 week before use allowed the Nafion membrane to equilibrate. Both the lactate and glucose sensors were stable for at least 6 months when stored at 4°C without any additional storing conditions. Before use, attachment of the NFC module to the wearable patch and exposure of glucose sensor to buffer solution [0.1 M sodium phosphate buffer (pH 7)] for 1 hour resulted in stabilized signals for micromolar detection in sweat. Lactate sensor required no such conditioning step.

Fabrication of battery-free NFC-based electronics

A LPKF U4 UV laser patterned a commercial substrate (DuPont Pyralux AP8535R) to form a flexible printed circuit board for the wireless, battery-free electronics. Pulsed mode electroplating (LPKF Contac S4) filled the vias with copper to form connections between the top and bottom layers of the device. The electronics assembly consisted of soldering the microcontroller and NFC front-end combination (TI RF430FRL152H), zero cross-over operational amplifier (ADA4505-2, Analog Devices), and various passive resistor and capacitor components in 0201 form factor, using low-temperature solder (In/Sn 90/10, Indium Corp.) paste. Last, a 14-µm-thick layer of parylene formed by chemical vapor deposition (SCS Labcoter 2 Parylene Deposition System; Specialty Coating Systems, IN) serves as a waterproof encapsulation for the entire system of NFC electronics.

Preparation of color reference markers

Calibration plots for each analyte resulted from exposure of chloride and pH assays to standard chloride and buffer solutions, capture of images of the assays using a digital single-lens reflex camera (EOS 6D; Canon, Tokyo, Japan), and image analysis (Photoshop, Adobe Systems, CA, USA). Thereafter, a color laser printer (C454 PS; Konica Minolta, Tokyo, Japan) produced color reference markers on transparent thin films of PET. Placing the color reference markers adjacent to the assay chambers and capturing images using a smartphone (iPhone 5s; Apple, CA, USA) enabled a comparison of color values (lightness value from Lab color space for chloride assay and R value from RGB color model for pH assay) of the reference markers with those of the assays. Adjusting the brightness of the color reference markers and repeated iteration resulted in optimized color reference markers with color values similar to colors from the assay chambers.

Color analysis for concentration estimation

1) Select three random spots in a chamber and calculate an average color value (C_{ch}) based on these three spots. In case of chloride, measure lightness L from Lab color space, while for pH, record R value from the RGB color model.

2) Follow same procedure as above to calculate the average color value from the reference markers on the left (CL_{ref}) and right (CR_{ref}) side of the chamber.

3) Calculate the mean (CM_{ref}) of CL_{ref} and CR_{ref}.

4) Compare C_{ch} to CM_{ref} to identify the smallest range ($CM_{ref,c1} < C_{ch} < CM_{ref,c2}$) in which C_{ch} lies.

5) Use Eq. 1 to estimate analyte concentration.

$$\text{conc. or pH} = \frac{C_{ch} - CM_{ref,c1}}{\left(\frac{CM_{ref,c2} - CM_{ref,c1}}{c2 - c1}\right)} + c1 \quad (1)$$

Experimental setup for electrochemical lactate and glucose sensors

Real-time signals for lactate and glucose sensors followed from measurements with sensors held at a given temperature on a hot plate and exposed to either buffer or artificial sweat (Pickering Laboratories, CA, USA), with no analyte to obtain a baseline reading using either a digital-to-analog converter (PowerLab 8/35; ADInstruments Inc., CO, USA) or the NFC electronic module. The artificial sweat contained several electrolytes, metabolites, amino acids, and vitamins, each at physiologically relevant concentrations. Serial addition and mixing of known concentrations of analyte into the buffer/artificial sweat using a pipette led to proportional increases in acquired voltage signal. Sensor signal stability studies involved suspending the sensor in a beaker containing buffer and spiking the solution with analyte under continuous mild stirring.

Data collection and analyses

Calibration plots for lactate and glucose sensors resulted from averaging real-time signals acquired in the last 30 s for each concentration for three separate sensors. Error bars in each plot indicate the SD of data from three separate sensors. During human trials, the subjects paused to take an image of the device using a smartphone camera, for colorimetric analysis. Mean values extracted from three random points ($n = 3$) from the colorimetric assays yielded the chloride concentration and pH. Mean concentration values calculated from the data generated by the electrochemical lactate and glucose sensors during the last 1 min ($n = 60$) of cycling resulted in concentrations.

SUPPLEMENTARY MATERIALS

Supplementary material for this article is available at http://advances.sciencemag.org/cgi/content/full/5/1/eaav3294/DC1

Fig. S1. Scheme illustrating integration of different device layers.
Fig. S2. Electrical characterization of the NFC electronic module.
Fig. S3. Benchtop characterization of biofuel cell–based lactate sensor.
Fig. S4. Benchtop characterization of biofuel cell–based glucose sensor.
Fig. S5. Mechanical resiliency studies.
Fig. S6. Protocol for concentration estimation for colorimetric assays.

Fig. S7. Effect of ambient lighting conditions and storage on accuracy of colorimetric assays.
Fig. S8. Scheme for microfluidics and typical NMR spectrum for sweat sample.
Fig. S9. Comparison of data acquired from sweat chloride sensors and that from HPLC.
Fig. S10. Two-day human trials.
Fig. S11. One-day human trials.
Fig. S12. Correlation between sweat concentration and blood levels.
Fig. S13. Sweat sensor stability and precision.
Table S1. Comparison of sensitivity and LOD for lactate and glucose sensors with that for previous examples.
Table S2. Comparison of data acquired from sensor patch and conventional techniques during human trials.
Movie S1. Demonstration of robust magnetic connection during vigorous movements.

REFERENCES AND NOTES

1. J. Heikenfeld, A. Jajack, J. Rogers, P. Gutruf, L. Tian, T. Pan, R. Li, M. Khine, J. Kim, J. Wang, Wearable sensors: Modalities, challenges, and prospects. *Lab Chip* **18**, 217–248 (2018).
2. A. J. Bandodkar, J. Wang, Non-invasive wearable electrochemical sensors: A review. *Trends Biotechnol.* **32**, 363–371 (2014).
3. J. Kim, A. S. Campbell, J. Wang, Wearable non-invasive epidermal glucose sensors: A review. *Talanta* **177**, 163–170 (2018).
4. T. Someya, Z. Bao, G. G. Malliaras, The rise of plastic bioelectronics. *Nature* **540**, 379–385 (2016).
5. J. A. Rogers, T. Someya, Y. Huang, Materials and mechanics for stretchable electronics. *Science* **327**, 1603–1607 (2010).
6. J. Kim, A. Banks, Z. Xie, S. Y. Heo, P. Gutruf, J. W. Lee, S. Xu, K.-I. Jang, F. Liu, G. Brown, J. Choi, J. H. Kim, X. Feng, Y. Huang, U. Paik, J. A. Rogers, Miniaturized flexible electronic systems with wireless power and near-field communication capabilities. *Adv. Funct. Mater.* **25**, 4761–4767 (2015).
7. N. Matsuhisa, D. Inoue, P. Zalar, H. Jin, Y. Matsuba, A. Itoh, T. Yokota, D. Hashizume, T. Someya, Printable elastic conductors by in situ formation of silver nanoparticles from silver flakes. *Nat. Mater.* **16**, 834–840 (2017).
8. A. J. Bandodkar, R. Nuñez-Flores, W. Jia, J. Wang, All-printed stretchable electrochemical devices. *Adv. Mater.* **27**, 3060–3065 (2015).
9. K. Chen, W. Gao, S. Emaminejad, D. Kiriya, H. Ota, H. Y. Y. Nyein, K. Takei, A. Javey, Printed carbon nanotube electronics and sensor systems. *Adv. Mater.* **28**, 4397–4414 (2016).
10. S. Ryu, P. Lee, J. B. Chou, R. Xu, R. Zhao, A. J. Hart, S.-G. Kim, Extremely elastic wearable carbon nanotube fiber strain sensor for monitoring of human motion. *ACS Nano* **9**, 5929–5936 (2015).
11. E. M. G. Rodrigues, R. Godina, C. M. P. Cabrita, J. P. S. Catalão, Experimental low cost reflective type oximeter for wearable health systems. *Biomed. Signal Process. Control* **31**, 419–433 (2017).
12. S. Imani, A. J. Bandodkar, A. M. V. Mohan, R. Kumar, S. Yu, J. Wang, P. P. Mercier, A wearable chemical–electrophysiological hybrid biosensing system for real-time health and fitness monitoring. *Nat. Commun.* **7**, 11650 (2016).
13. B. C.-K. Tee, A. Chortos, R. R. Dunn, G. Schwartz, E. Eason, Z. Bao, Tunable flexible pressure sensors using microstructured elastomer geometries for intuitive electronics. *Adv. Funct. Mater.* **24**, 5427–5434 (2014).
14. S. Krishnan, Y. Shi, R. C. Webb, Y. Ma, P. Bastien, K. E. Crawford, A. Wang, X. Feng, M. Manco, J. Kurniawan, E. Tir, Y. Huang, G. Balooch, R. M. Pielak, J. A. Rogers, Multimodal epidermal devices for hydration monitoring. *Microsyst. Nanoeng.* **3**, 17014 (2017).
15. T. F. O'Connor, M. E. Fach, R. Miller, S. E. Root, P. P. Mercier, D. J. Lipomi, The language of glove: Wireless gesture decoder with low-power and stretchable hybrid electronics. *PLOS ONE* **12**, e0179766 (2017).
16. E. Higurashi, R. Sawada, T. Ito, An integrated laser blood flowmeter. *J. Lightwave Technol.* **21**, 591–595 (2003).
17. S. Yang, Y.-C. Chen, L. Nicolini, P. Pasupathy, J. Sacks, B. Su, R. Yang, D. Sanchez, Y.-F. Chang, P. Wang, D. Schnyer, D. Neikirk, N. Lu, "Cut-and-paste" manufacture of multiparametric epidermal sensor systems. *Adv. Mater.* **27**, 6423–6430 (2015).
18. J. Heikenfeld, Non-invasive analyte access and sensing through eccrine sweat: Challenges and outlook circa 2016. *Electroanalysis* **28**, 1242–1249 (2016).
19. G. Matzeu, L. Florea, D. Diamond, Advances in wearable chemical sensor design for monitoring biological fluids. *Sens. Actuators B* **211**, 403–418 (2015).
20. W. S. E. Gao, H. Y. Y. Nyein, S. Challa, K. Chen, A. Peck, H. M. Fahad, H. Ota, H. Shiraki, D. Kiriya, D.-H. Lien, G. A. Brooks, R. W. Davis, A. Javey, Fully integrated wearable sensor arrays for multiplexed in situ perspiration analysis. *Nature* **529**, 509–514 (2016).
21. A. Koh, D. Kang, Y. Xue, S. Lee, R. M. Pielak, J. Kim, T. Hwang, S. Min, A. Banks, P. Bastien, M. C. Manco, L. Wang, K. R. Ammann, K.-I. Jang, P. Won, S. Han, R. Ghaffari, U. Paik, M. J. Slepian, G. Balooch, Y. Huang, J. A. Rogers, A soft, wearable microfluidic device for the capture, storage, and colorimetric sensing of sweat. *Sci. Transl. Med.* **8**, 366ra165 (2016).
22. S. Biagi, S. Ghimenti, M. Onor, E. Bramanti, Simultaneous determination of lactate and pyruvate in human sweat using reversed-phase high-performance liquid chromatography: A noninvasive approach. *Biomed. Chromatogr.* **26**, 1408–1415 (2012).
23. W. Jia, A. J. Bandodkar, G. Valdés-Ramírez, J. R. Windmiller, Z. Yang, J. Ramírez, G. Chan, J. Wang, Electrochemical tattoo biosensors for real-time noninvasive lactate monitoring in human perspiration. *Anal. Chem.* **85**, 6553–6560 (2013).
24. A. Martín, J. Kim, J. F. Kurniawan, J. R. Sempionatto, J. R. Moreto, G. Tang, A. S. Campbell, A. Shin, M. Y. Lee, X. Liu, J. Wang, Epidermal microfluidic electrochemical detection system: Enhanced sweat sampling and metabolite detection. *ACS Sens.* **2**, 1860–1868 (2017).
25. A. Abellán-Llobregat, I. Jeerapan, A. Bandodkar, L. Vidal, A. Canals, J. Wang, E. Morallón, A stretchable and screen-printed electrochemical sensor for glucose determination in human perspiration. *Biosens. Bioelectron.* **91**, 885–891 (2017).
26. H. Lee, T. K. Choi, Y. B. Lee, H. R. Cho, R. Ghaffari, L. Wang, H. J. Choi, T. D. Chung, N. Lu, T. Hyeon, S. H. Choi, D.-H. Kim, A graphene-based electrochemical device with thermoresponsive microneedles for diabetes monitoring and therapy. *Nat. Nanotechnol.* **11**, 566–572 (2016).
27. S. Y. Oh, S. Y. Hong, Y. R. Jeong, J. Yun, H. Park, S. W. Jin, G. Lee, J. H. Oh, H. Lee, S.-S. Lee, J. S. Ha, Skin-attachable, stretchable electrochemical sweat sensor for glucose and pH detection. *ACS Appl. Mater. Interfaces* **10**, 13729–13740 (2018).
28. S. J. Montain, M. N. Sawka, C. B. Wenger, Hyponatremia associated with exercise: Risk factors and pathogenesis. *Exerc. Sport Sci. Rev.* **29**, 113–117 (2001).
29. S. Wang, G. Zhang, H. Meng, L. Li, Effect of exercise-induced sweating on facial sebum, stratum corneum hydration, and skin surface pH in normal population. *Skin Res. Technol.* **19**, e312–e317 (2013).
30. S. F. Godek, A. R. Bartolozzi, J. J. Godek, Sweat rate and fluid turnover in American football players compared with runners in a hot and humid environment. *Br. J. Sports Med.* **39**, 205–211 (2005).
31. B. Schazmann, D. Morris, C. Slater, S. Beirne, C. Fay, R. Reuveny, N. Moyna, D. Diamond, A wearable electrochemical sensor for the real-time measurement of sweat sodium concentration. *Anal. Methods* **2**, 342–348 (2010).
32. J. Hu, A. Stein, P. Bühlmann, Rational design of all-solid-state ion-selective electrodes and reference electrodes. *Trends Analyt. Chem.* **76**, 102–114 (2016).
33. D. P. Rose, M. E. Ratterman, D. K. Griffin, L. Hou, N. Kelley-Loughnane, R. R. Naik, J. A. Hagen, I. Papautsky, J. C. Heikenfeld, Adhesive RFID sensor patch for monitoring of sweat electrolytes. *IEEE Trans. Biomed. Eng.* **62**, 1457–1465 (2015).
34. I. Jeerapan, J. R. Sempionatto, A. Pavinatto, J.-M. You, J. Wang, Stretchable biofuel cells as wearable textile-based self-powered sensors. *J. Mater. Chem. A* **4**, 18342–18353 (2016).
35. G. Valdés-Ramírez, Y.-C. Li, J. Kim, W. Jia, A. J. Bandodkar, R. Nuñez-Flores, P. R. Miller, S.-Y. Wu, R. Narayan, J. R. Windmiller, R. Polsky, J. Wang, Microneedle-based self-powered glucose sensor. *Electrochem. Commun.* **47**, 58–62 (2014).
36. S. Emaminejad, W. Gao, E. Wu, Z. A. Davies, H. Yin Yin Nyein, S. Challa, S. P. Ryan, H. M. Fahad, K. Chen, Z. Shahpar, S. Talebi, C. Milla, A. Javey, R. W. Davis, Autonomous sweat extraction and analysis applied to cystic fibrosis and glucose monitoring using a fully integrated wearable platform. *Proc. Natl. Acad. Sci. U.S.A.* **114**, 4625–4630 (2017).
37. A. J. Bandodkar, V. W. Hung, W. Jia, G. Valdés-Ramírez, J. R. Windmiller, A. G. Martinez, J. Ramírez, G. Chan, K. Kerman, J. Wang, Tattoo-based potentiometric ion-selective sensors for epidermal pH monitoring. *Analyst* **138**, 123–128 (2013).
38. C. J. Harvey, R. F. LeBouf, A. B. Stefaniak, Formulation and stability of a novel artificial human sweat under conditions of storage and use. *Toxicol. In Vitro* **24**, 1790–1796 (2010).
39. J. Choi, R. Ghaffari, L. B. Baker, J. A. Rogers, Skin-interfaced systems for sweat collection and analytics. *Sci. Adv.* **4**, eaar3921 (2018).
40. J. Choi, D. Kang, S. Han, S. B. Kim, J. A. Rogers, Thin, soft, skin-mounted microfluidic networks with capillary bursting valves for chrono-sampling of sweat. *Adv. Healthc. Mater.* **6**, 1601355 (2017).
41. J. E. Barney, R. J. Bertolacini, Colorimetric determination of chloride with mercuric chloranilate. *Anal. Chem.* **29**, 1187–1188 (1957).
42. H. Araki, J. Kim, S. Zhang, A. Banks, K. E. Crawford, X. Sheng, P. Gutruf, Y. Shi, R. M. Pielak, J. A. Rogers, Materials and device designs for an epidermal UV colorimetric dosimeter with near field communication capabilities. *Adv. Funct. Mater.* **27**, 1604465 (2017).
43. S. B. Kim, Y. Zhang, S. M. Won, A. J. Bandodkar, Y. Sekine, Y. Xue, J. Koo, S. W. Harshman, J. A. Martin, J. M. Park, T. R. Ray, K. E. Crawford, K.-T. Lee, J. Choi, R. L. Pitsch, C. C. Grigsby, A. J. Strang, Y.-Y. Chen, S. Xu, J. Kim, A. Koh, J. S. Ha, Y. Huang, S. W. Kim, J. A. Rogers, Super-absorbent polymer valves and colorimetric chemistries for time-sequenced discrete sampling and chloride analysis of sweat via skin-mounted soft microfluidics. *Small* **14**, e1703334 (2018).
44. A. Mishra, R. Greaves, J. Massie, The relevance of sweat testing for the diagnosis of cystic fibrosis in the genomic era. *Clin. Biochem. Rev.* **26**, 135–153 (2005).
45. J. Choi, Y. Xue, W. Xia, T. R. Ray, J. T. Reeder, A. J. Bandodkar, D. Kang, S. Xu, Y. Huang, J. A. Rogers, Soft, skin-mounted microfluidic systems for measuring secretory fluidic

pressures generated at the surface of the skin by eccrine sweat glands. *Lab Chip* **17**, 2572–2580 (2017).
46. S. Palipana, B. Pietropaoli, D. Pesch, Recent advances in RF-based passive device-free localisation for indoor applications. *Ad Hoc Netw.* **64**, 80–98 (2017).
47. S. F. Wong, H. C. Mak, C. H. Ku, W. I. Ho, Developing advanced traffic violation detection system with RFID technology for smart city, in *2017 IEEE International Conference on Industrial Engineering and Engineering Management (IEEM)*, 10 to 13 December 2017 (IEEE, 2017), pp. 334–338.
48. M. Harker, H. Coulson, I. Fairweather, D. Taylor, C. A. Daykin, Study of metabolite composition of eccrine sweat from healthy male and female human subjects by ^{1}H NMR spectroscopy. *Metabolomics* **2**, 105–112 (2006).
49. V. A. LeGrys, J. R. Yankaskas, L. M. Quittell, B. C. Marshall, P. J. Mogayzel Jr.; Cystic Fibrosis Foundation, Diagnostic sweat testing: The cystic fibrosis foundation guidelines. *J. Pediatr.* **151**, 85–89 (2007).
50. M. S. Boyne, D. M. Silver, J. Kaplan, C. D. Saudek, Timing of changes in interstitial and venous blood glucose measured with a continuous subcutaneous glucose sensor. *Diabetes* **52**, 2790–2794 (2003).
51. A. J. Bandodkar, W. Jia, J. Ramírez, J. Wang, Biocompatible enzymatic roller pens for direct writing of biocatalytic materials:"do-it-yourself" electrochemical biosensors. *Adv. Healthc. Mater.* **4**, 1215–1224 (2015).

Acknowledgments: We would like to acknowledge Y. Zhang at Integrated Molecular Structure Education and Research Center, Northwestern University for assistance in NMR analysis and Keck Biophysics Facility and the Stupp Laboratory, Northwestern University for access to lyophilizer. **Funding:** This research was funded by the Air Force Research Laboratory (AFRL) Human Signatures Branch through core funds provided to Northwestern University under contract FA8650-14-D-6516. This work used the Northwestern University Micro/Nano Fabrication Facility (NUFAB), which is partially supported by Soft and Hybrid Nanotechnology Experimental (SHyNE) Resource (NSF ECCS-1542205), the Materials Research Science and Engineering Center (DMR-1720139), the State of Illinois, and Northwestern University. **Author contributions:** J.A.R., A.J.B., P.G., and J.C. conceived the project, designed the studies, and analyzed and interpreted data. A.J.B. developed the pH, lactate, and glucose sensors. P.G. developed the NFC electronics. J.C. developed the microfluidics. J.C., A.J.A., S.P.L., J.B.M., and R.G. developed and analyzed chloride assay. K.L., C.-J.S., J.P.L., and V.K. assisted in NFC electronic fabrication. Y.S., A.V., and K.T. assisted in the sensor fabrication. W.J.J., T.R., J.T.R., S.H., and J.K. assisted in microfluidic fabrication. A.J.B., P.G., and J.C. conducted the experiments. T.H. assisted in performing human trials. J.A.R., A.J.B., P.G., J.C., W.J.J., T.R., S.K., and R.G. wrote the manuscript. **Competing interests:** J.A.R., R.G., A.J.A., S.P.L., and J.B.M. are co-founders of Epicore Biosystems Inc., a company that pursues commercialization of microfluidic devices for wearable applications. J.A.R., A.J.B., J.T.R., Y.S., J.C., T.R., P.G., and K.L. are inventors on a patent related to this work filed by the U.S. Patent and Trademark Office (no. PCT/US2018/035738, filed 1 June 2018). J.A.R., A.J.B., J.T.R., Y.S., J.C., and T.R. are inventors on another patent related to this work filed by the U.S. Patent and Trademark Office (no. PCT/US2018/035661, filed 1 June 2018). The other authors declare that they have no competing interests. **Data and materials availability:** All data needed to evaluate the conclusions in the paper are present in the paper and/or the Supplementary Materials. Additional data related to this paper may be requested from the authors.

Submitted 5 September 2018
Accepted 6 December 2018
Published 18 January 2019
10.1126/sciadv.aav3294

Citation: A. J. Bandodkar, P. Gutruf, J. Choi, KH. Lee, Y. Sekine, J. T. Reeder, W. J. Jeang, A. J. Aranyosi, S. P. Lee, J. B. Model, R. Ghaffari, C.-J. Su, J. P. Leshock, T. Ray, A. Verrillo, K. Thomas, V. Krishnamurthi, S. Han, J. Kim, S. Krishnan, T. Hang, J. A. Rogers, Battery-free, skin-interfaced microfluidic/electronic systems for simultaneous electrochemical, colorimetric, and volumetric analysis of sweat. *Sci. Adv.* **5**, eaav3294 (2019).

ScienceAdvances

Battery-free, skin-interfaced microfluidic/electronic systems for simultaneous electrochemical, colorimetric, and volumetric analysis of sweat

Amay J. Bandodkar, Philipp Gutruf, Jungil Choi, KunHyuck Lee, Yurina Sekine, Jonathan T. Reeder, William J. Jeang, Alexander J. Aranyosi, Stephen P. Lee, Jeffrey B. Model, Roozbeh Ghaffari, Chun-Ju Su, John P. Leshock, Tyler Ray, Anthony Verrillo, Kyle Thomas, Vaishnavi Krishnamurthi, Seungyong Han, Jeonghyun Kim, Siddharth Krishnan, Tao Hang and John A. Rogers

Sci Adv **5** (1), eaav3294.
DOI: 10.1126/sciadv.aav3294

Supplementary Materials for

Battery-free, skin-interfaced microfluidic/electronic system for simultaneous electrochemical, colorimetric & volumetric sweat analysis

Amay J. Bandodkar, Philipp Gutruf, Jungil Choi, KunHyuck Lee, Yurina Sekine, Jonathan T. Reeder, William J. Jeang, Alexander J. Aranyosi, Stephen P. Lee, Jeffrey B. Model, Roozbeh Ghaffari, Chun-Ju Su, John P. Leshock, Tyler Ray, Anthony Verrillo, Kyle Thomas, Vaishnavi Krishnamurthi, Seungyong Han, Jeonghyun Kim, Siddharth Krishnan, Tao Hang and John A. Rogers

This PDF includes:

Fig. S7. Comparison of analyte concentration estimated using (A, B) chloride and (C, D) pH assay under various lighting conditions. Optical images of chloride assay on (E) Day 0 and (F) after 2 days and of pH assay on (G) Day 0 and (H) after 2 days. (I) Relationship between normalized total sweat loss and volume captured in sweat rate sensor. (Photo credit: Jungil Choi, Northwestern University)

Fig. S8. (A) Schematic illustration of capillary bursting valves in a colorimetric detection chamber. (B) Schematic illustration of microfluidic channel: 1) Glucose detection chamber 2) lactate detection chamber 3) chloride chrono detection chambers 4) pH chrono detection chambers 5) sweat rate detection chamber. (C) A typical NMR spectrum for sweat sample collected from Subject #1.

Fig. S9. Comparison of data acquired from sweat chloride sensors and that from HPLC.

Fig. S10. Correlation of data acquired from biofuel cell-based glucose and lactate sweat sensors with that acquired from blood glucose and lactate meter respectively over a period of two days for (A) subject #2 and (B) subject #3. (Photo credit: Philipp Gutruf, Northwestern University)

Fig. S11. Correlation of data acquired from biofuel cell-based glucose and lactate sweat sensors with that acquired from blood glucose and lactate meter respectively over a period of one day for subject #2 (with time lag compensation).

Fig. S12. Comparison of sweat sensor responses to lactate and glucose to concentrations determined in the blood levels using commercial instruments for (A, B) subject #1 (based on data reported in Fig. 7B) and (C, D) subject #2 (based on data reported in Fig. S11).

Fig. S13. (A) Comparison of signal of fresh, unused glucose sensor (black) with that obtained from one after two-day human trial (red) when exposed to 300μM glucose solution. (B) Comparison of signal of fresh, unused lactate sensor (black) with that obtained from one after two-day human trial (red) when exposed to 10mM lactate solution. Two-day human trails study comparing sweat sensor signals with that from NMR for (C) glucose and (D) lactate. (M: morning; E: evening). Benchtop stability studies of (E) glucose (100 μM) and (F) lactate (5 mM) sensors using artificial sweat at a temperature 30 ± 3 °C with the device bent to a radius of curvature of 35 mm.

Table S1. Comparison of sensitivity and LOD for lactate and glucose sensor with that for previous examples.

Table S2. Comparison of data acquired from sensor patch and conventional techniques during human trials.

Movie S1. Demonstration of robust magnetic connection during vigorous movements.

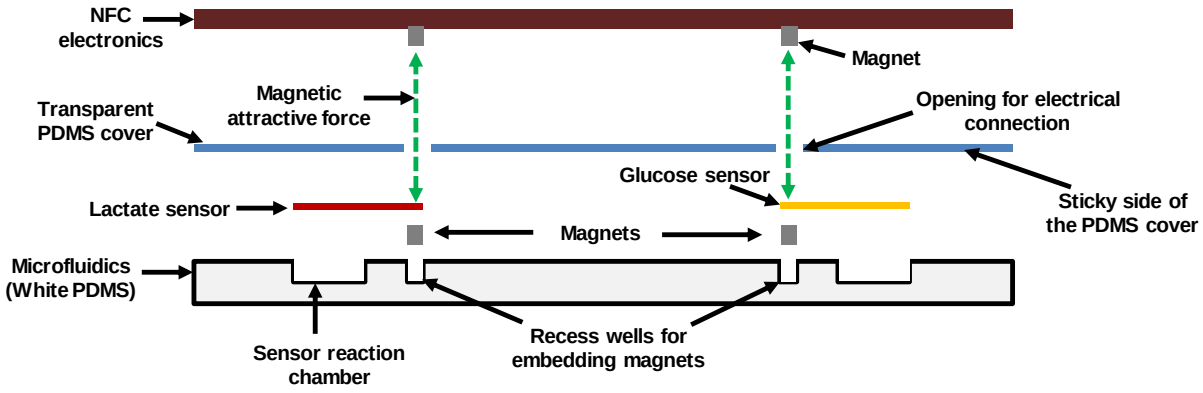

Fig. S1. Scheme illustrating integration of different device layers.

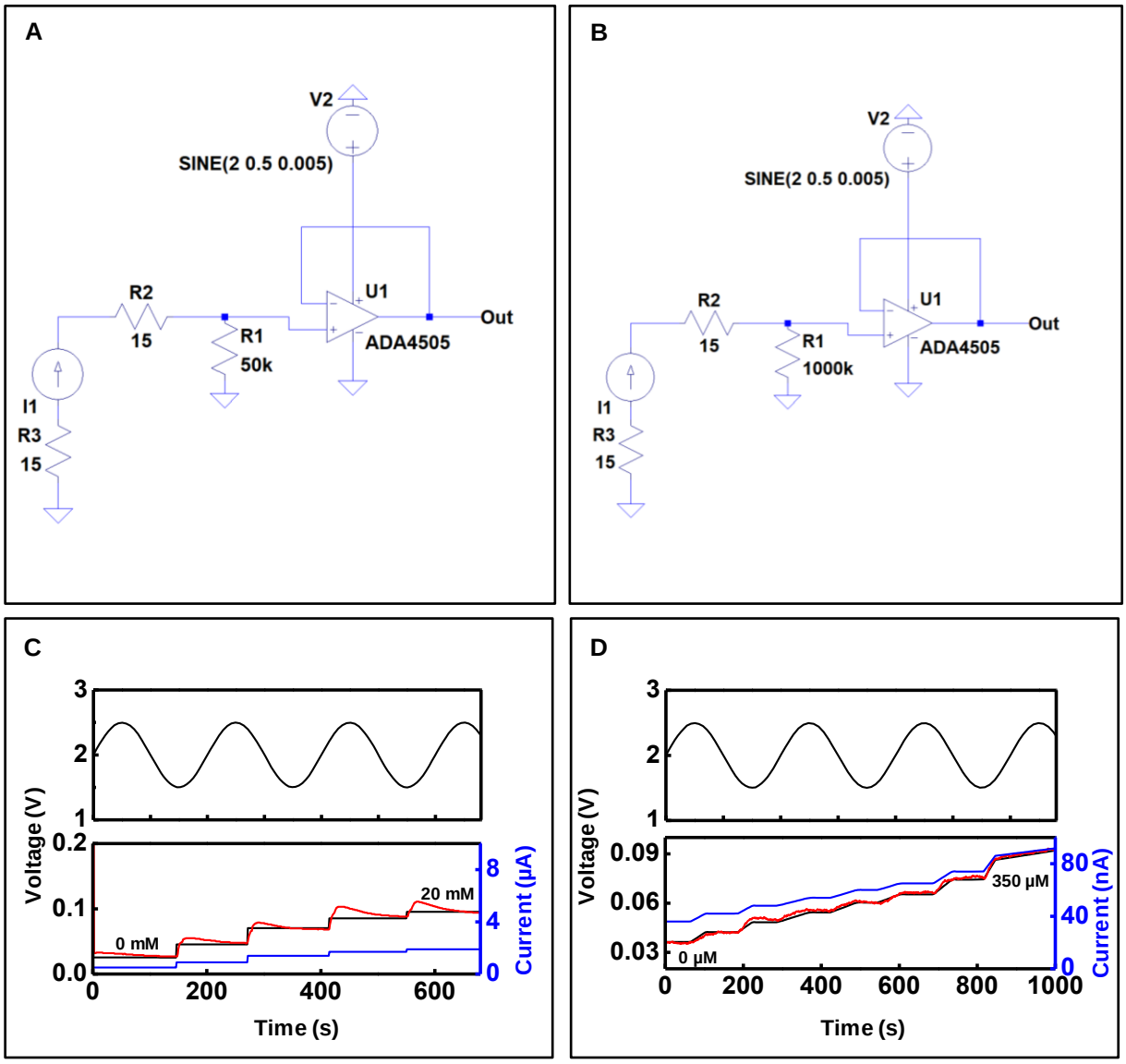

Fig. S2. (A and B) SPICE schematic of amplification scheme where R3 and R2 represent contact resistance of magnetic connection and R1 represents the respective load for (A) lactate and (B) glucose biofuel cell-based sensor. (C-D) Simulation results for amplified signal (black trace for voltage and blue trace for sensor current) vs. benchtop measurements (red trace) with oscillating supply voltage; demonstrating supply voltage insensitivity for (C) lactate and (D) glucose measurements with increasing concentrations.

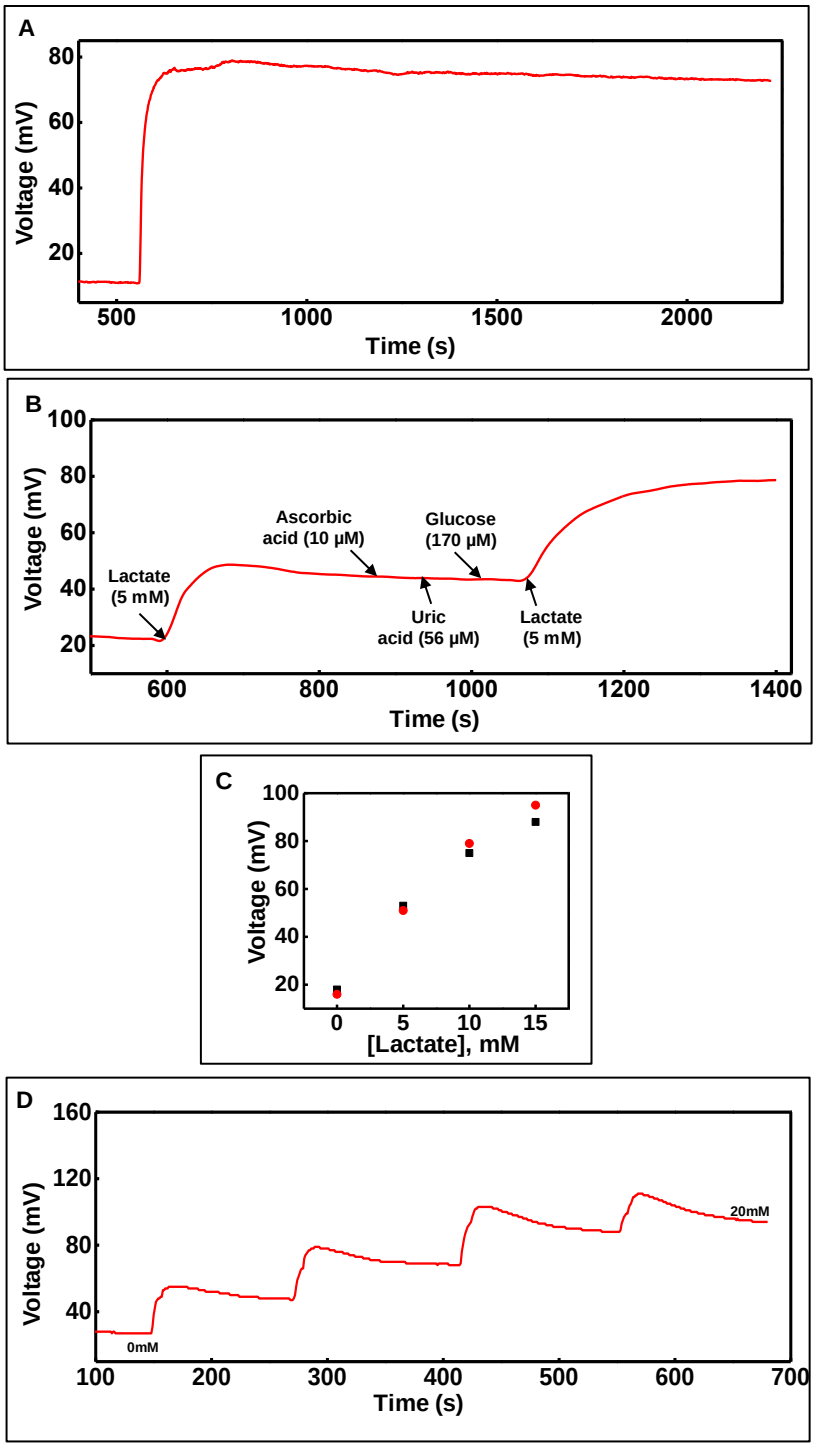

Fig. S3. Signal (A) stability (when exposed to 10mM lactate) and (B) interference study in presence of common interfering species for lactate sensor. (C) Calibration plot for lactate sensor for two consecutive cycles of reversibly changing concentration between 0-15 mM (maximum R.S.D. ~ 5.5%). (D) Real-time sensor response to increasing lactate concentration in phosphate buffer (pH 7.0) at 37 ± 3 °C.

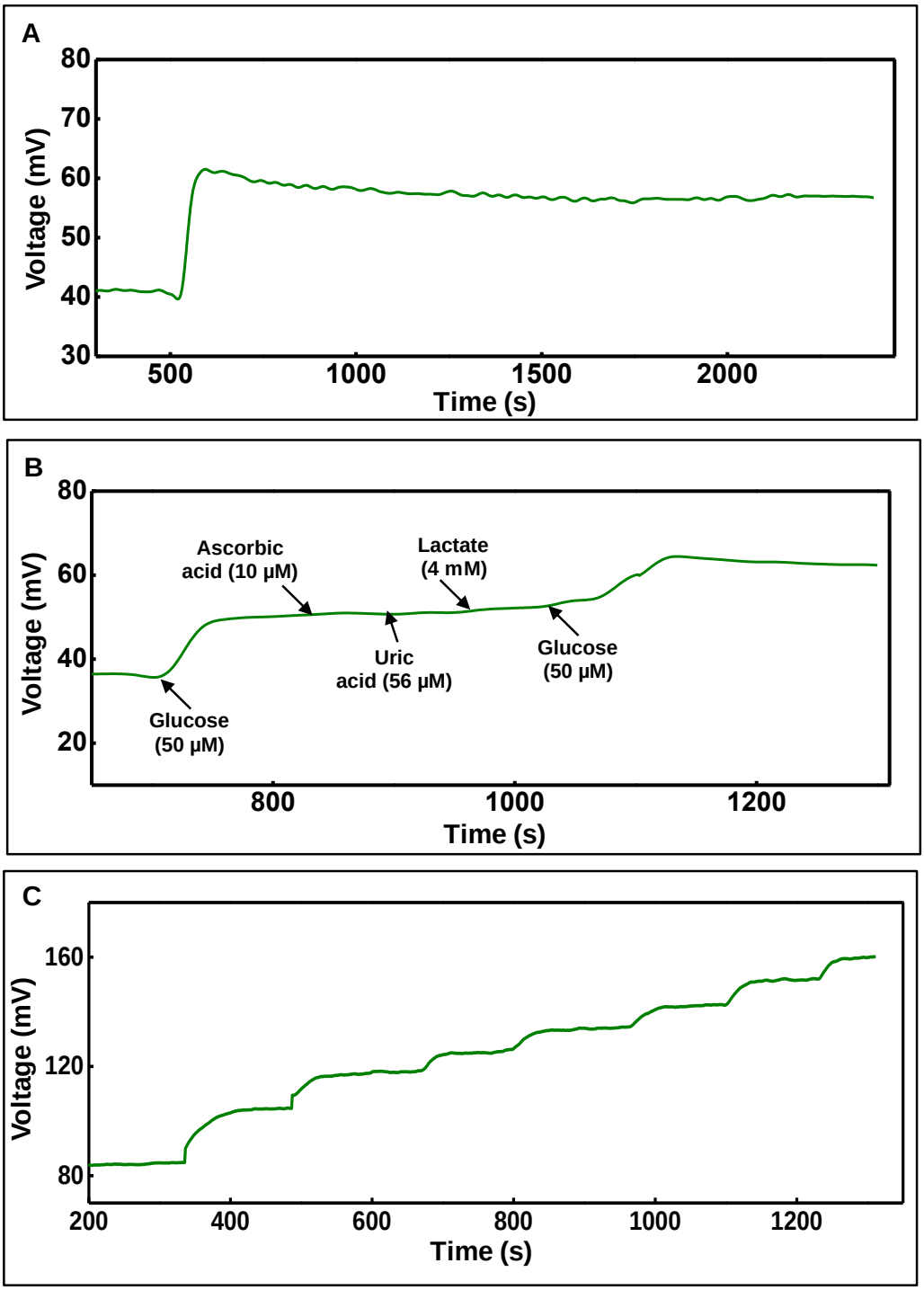

Fig. S4. Signal (A) stability (when exposed to 150 μM glucose) and (B) interference study in presence of common interfering species for glucose sensor. (C) Real-time sensor response to increasing glucose concentration in phosphate buffer (pH 7.0) at 37 ± 3 °C.

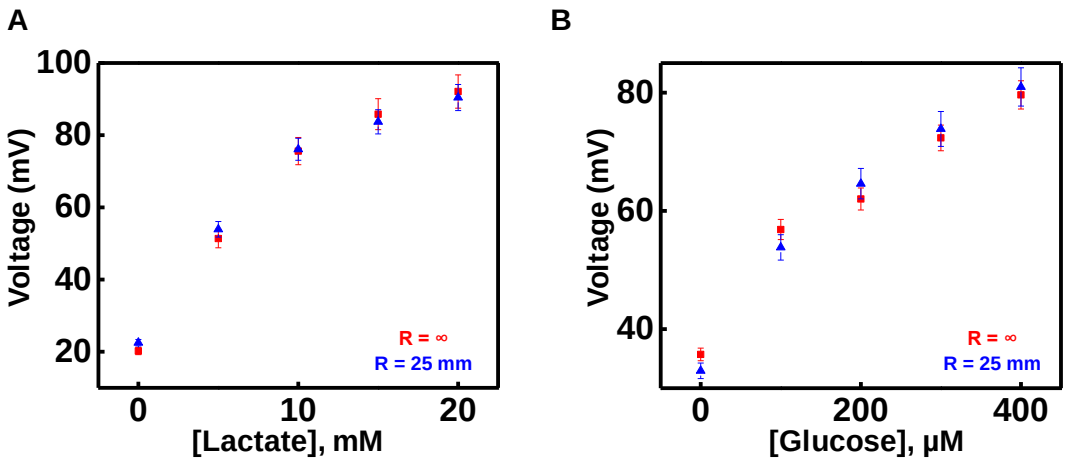

Fig. S5. Effect of bending on (A) lactate and (B) glucose sensor response.

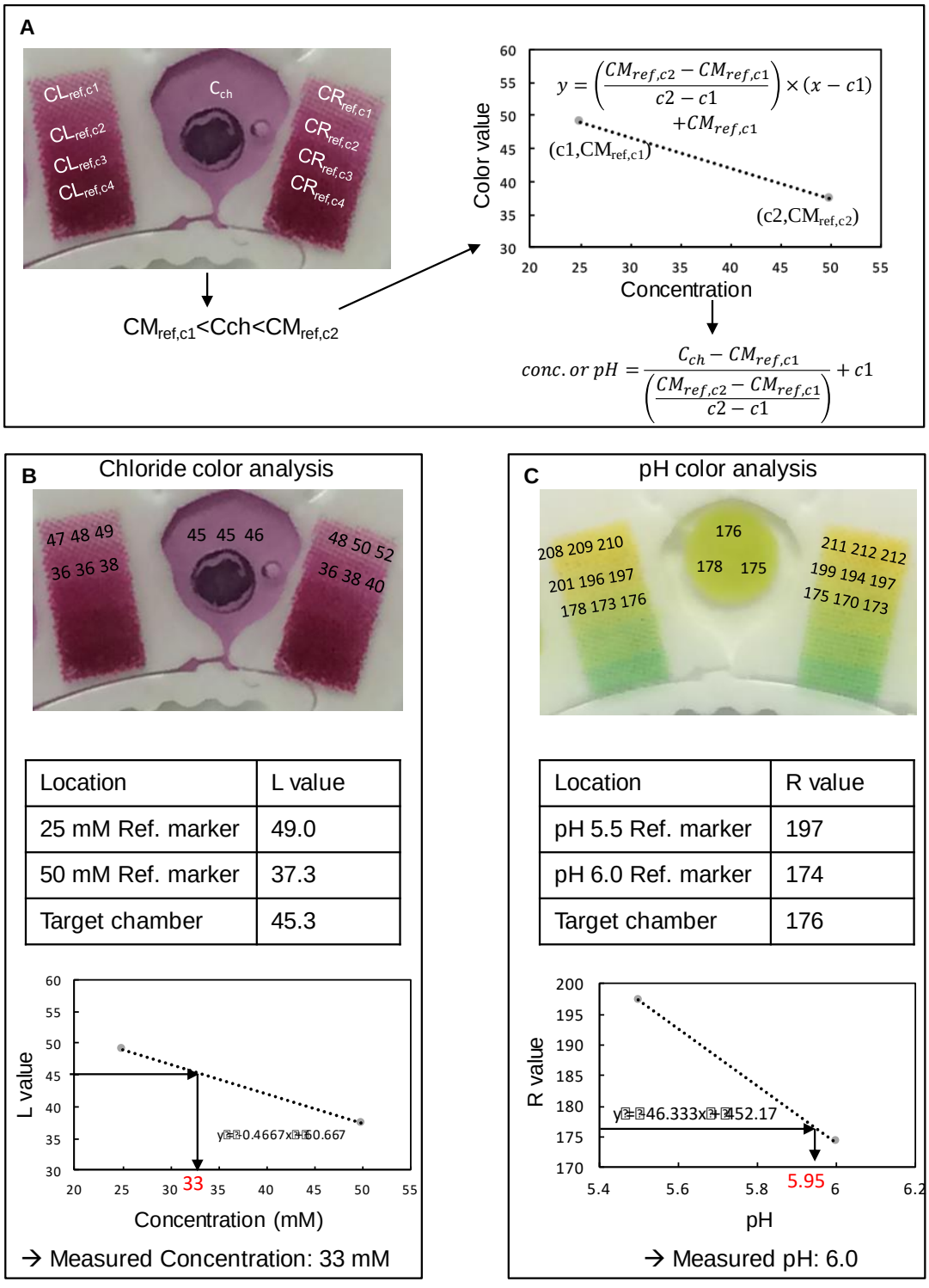

Fig. S6. (A) General protocol to analyze the concentration or pH from the color values from assay chamber and color reference marker. Examples of measuring color from (B) chloride assay chamber and (C) pH assay chamber. (Photo credit: Jungil Choi, Northwestern University)

A

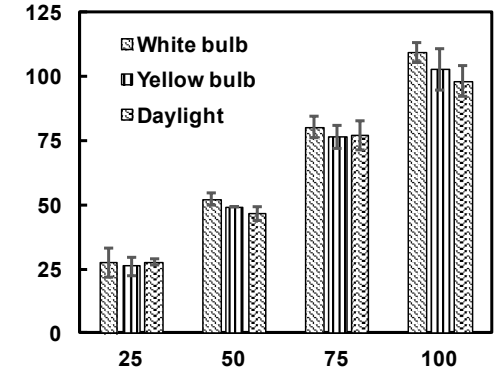

B

		concentrations (mM)			
	Chloride	25	50	75	100
White bulb light	Measured	27	52	80	109
	S.D.	6	2	4	4
	Max Error	8	4	9	13
Yellow bulb light	Measured	26	49	76	103
	S.D.	3	0	4	8
	Max Error	4	1	5	11
Daylight	Measured	28	47	77	98
	S.D.	1	3	6	6
	Max Error	4	6	8	8

C

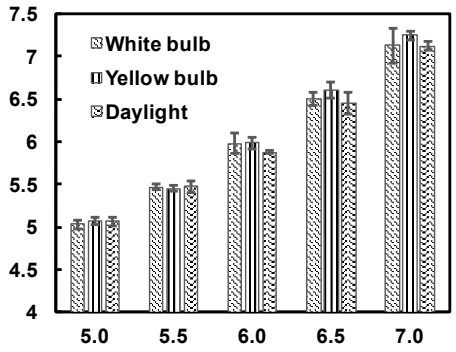

D

		pH				
	pH	5.0	5.5	6.0	6.5	7.0
White bulb light	Measured	5.0	5.5	6.0	6.5	7.1
	S.D.	0.05	0.03	0.12	0.08	0.20
	Max Error	0.05	0.03	0.12	0.08	0.3
Yellow bulb light	Measured	5.1	5.5	6.0	6.6	7.2
	S.D.	0.04	0.03	0.07	0.09	0.05
	Max Error	0.14	0.03	0.07	0.19	0.25
Daylight	Measured	5.1	5.5	5.9	6.4	7.1
	S.D.	0.05	0.07	0.02	0.13	0.05
	Max Error	0.15	0.07	0.12	0.23	0.15

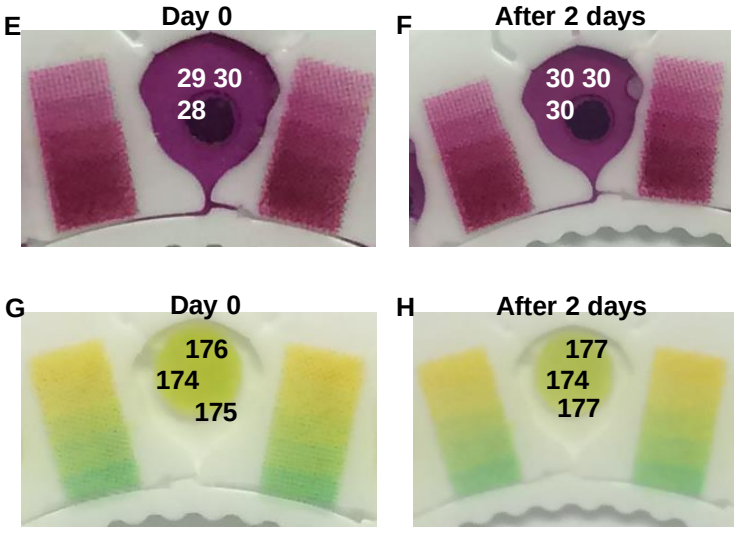

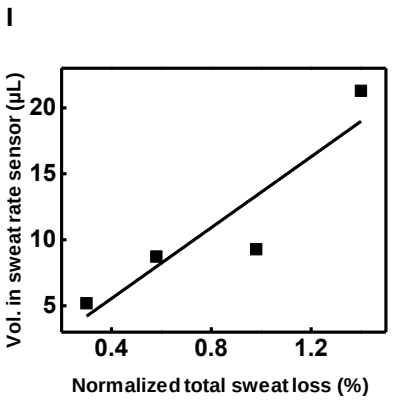

Fig. S7. Comparison of analyte concentration estimated using (A, B) chloride and (C, D) pH assay under various lighting conditions. Optical images of chloride assay on (E) Day 0 and (F) after 2 days and of pH assay on (G) Day 0 and (H) after 2 days. (I) Relationship between normalized total sweat loss and volume captured in sweat rate sensor. (Photo credit: Jungil Choi, Northwestern University)

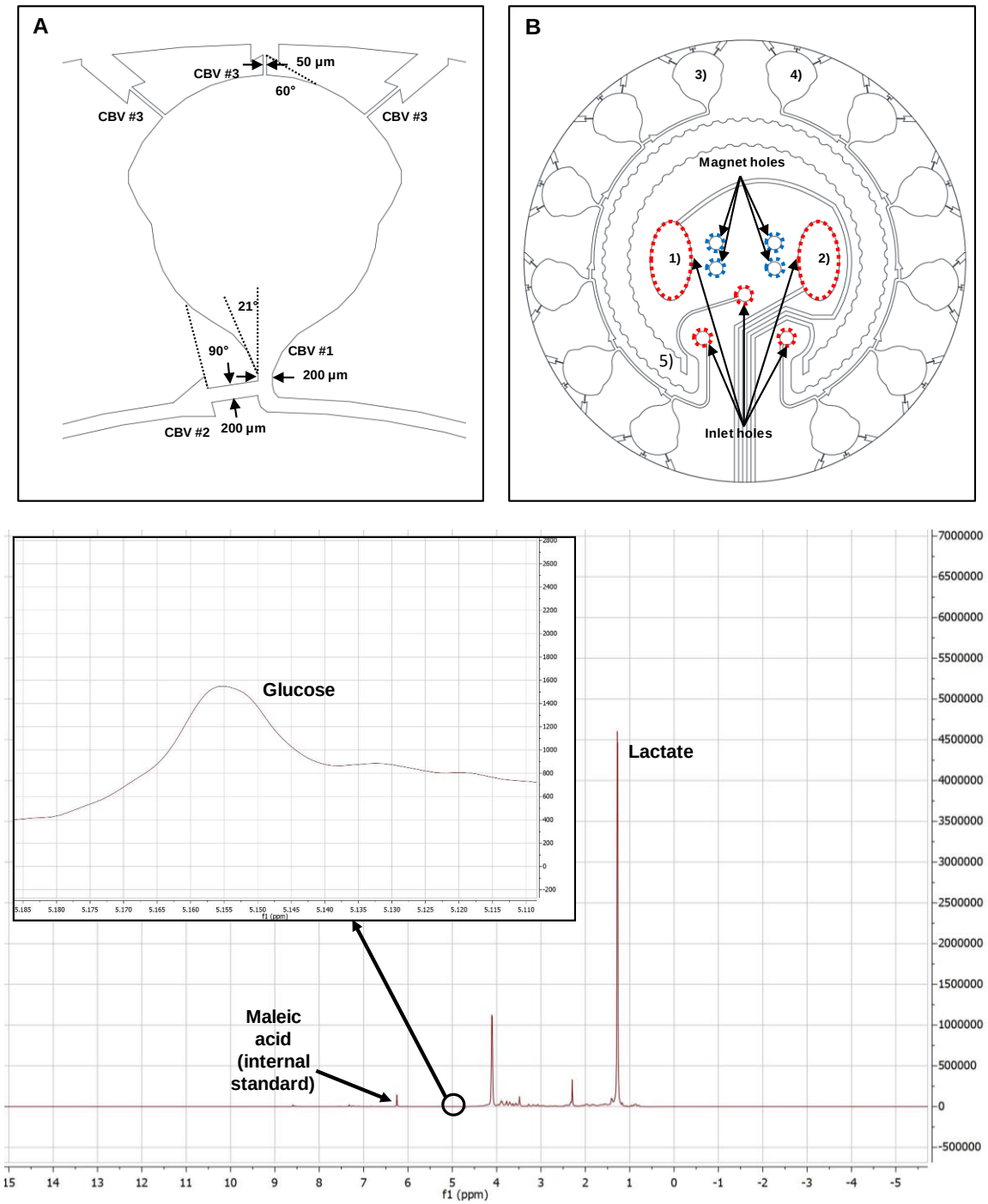

Fig. S8. (A) Schematic illustration of capillary bursting valves in a colorimetric detection chamber. (B) Schematic illustration of microfluidic channel: 1) Glucose detection chamber 2) lactate detection chamber 3) chloride chrono detection chambers 4) pH chrono detection chambers 5) sweat rate detection chamber. (C) A typical NMR spectrum for sweat sample collected from Subject #1.

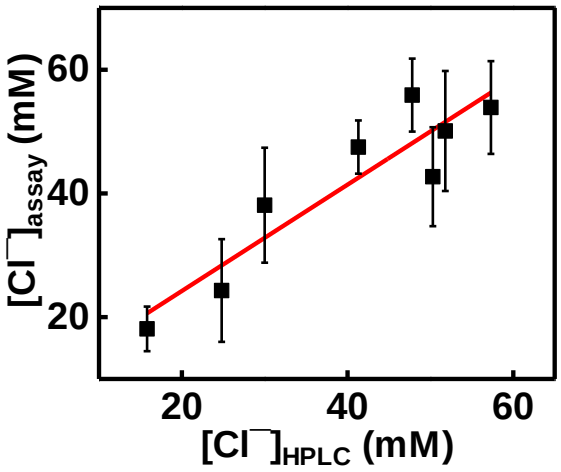

Fig. S9. Comparison of data acquired from sweat chloride sensors and that from HPLC.

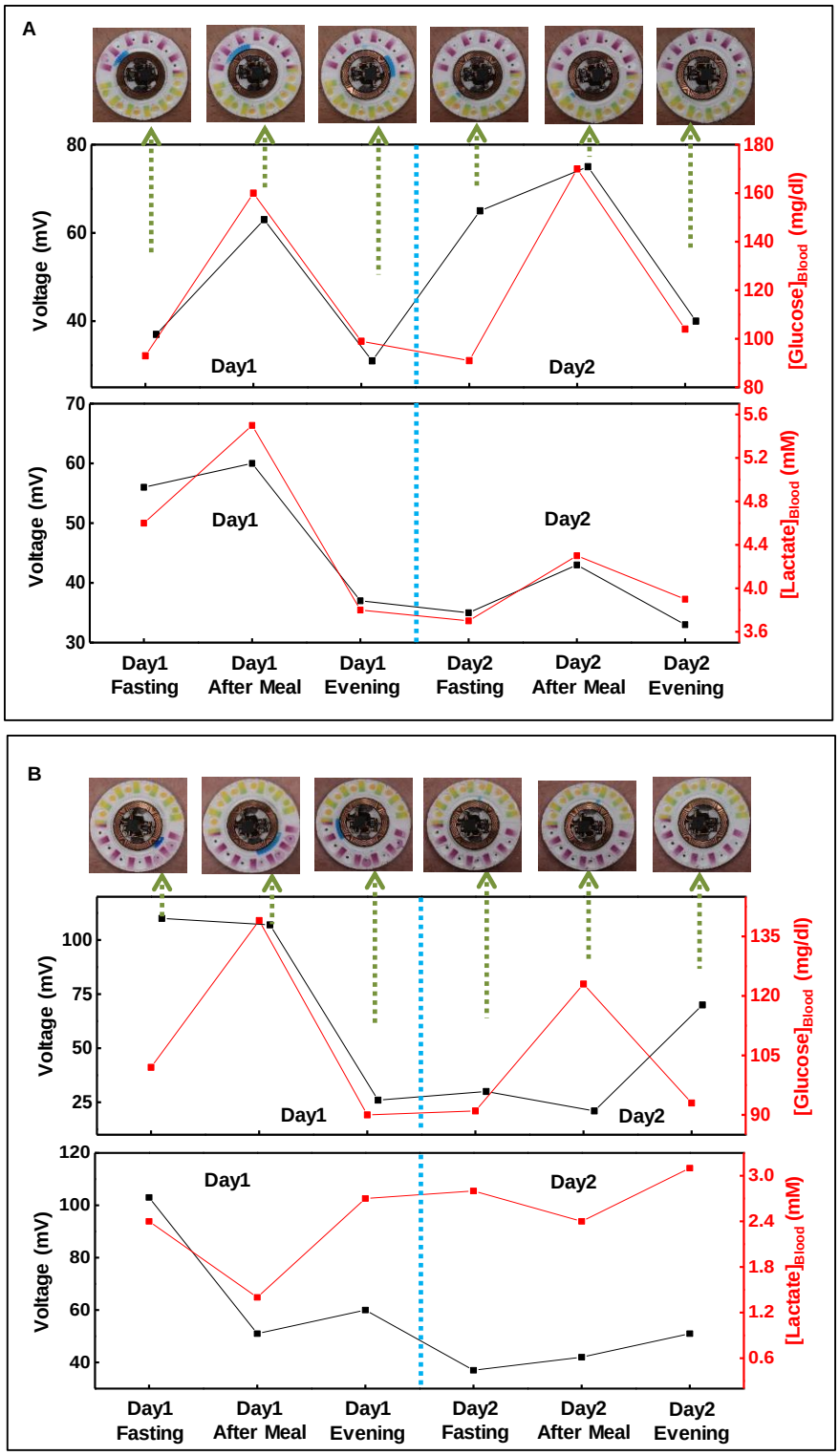

Fig. S10. Correlation of data acquired from biofuel cell-based glucose and lactate sweat sensors with that acquired from blood glucose and lactate meter respectively over a period of two days for (A) subject #2 and (B) subject #3. (Photo credit: Philipp Gutruf, Northwestern University)

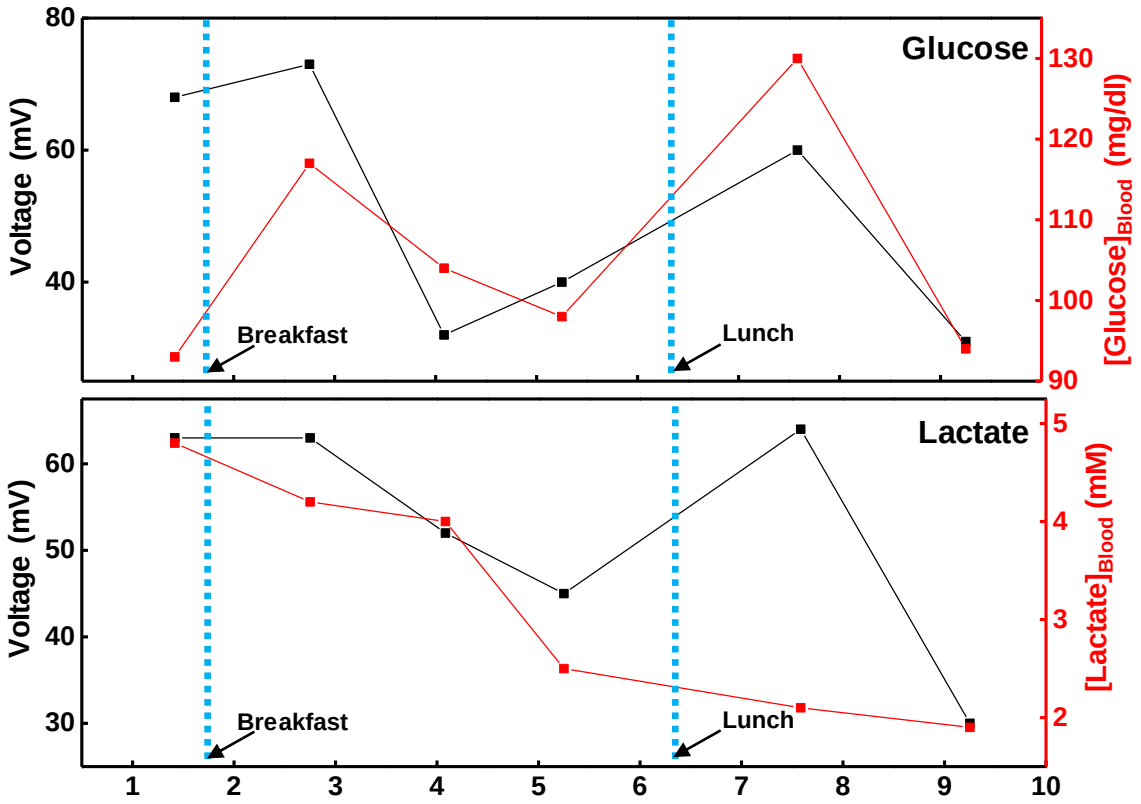

Fig. S11. Correlation of data acquired from biofuel cell-based glucose and lactate sweat sensors with that acquired from blood glucose and lactate meter respectively over a period of one day for subject #2 (with time lag compensation).

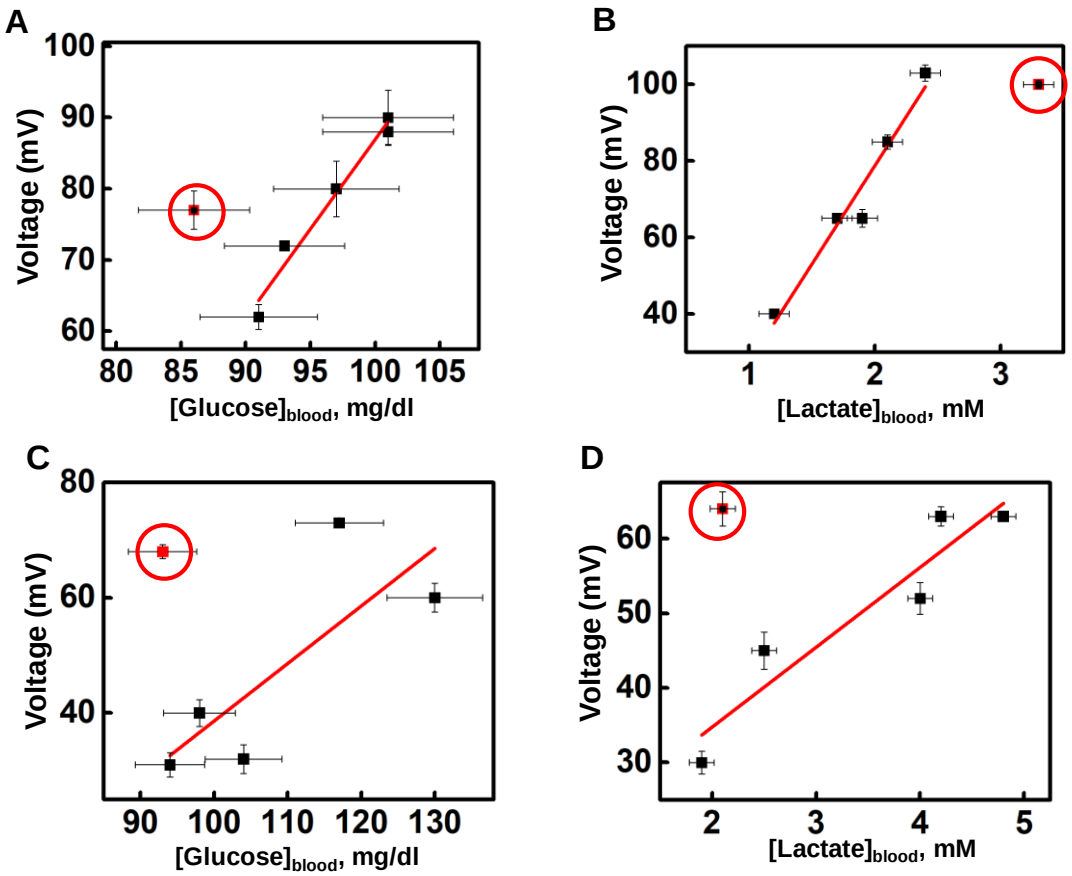

Fig. S12. Comparison of sweat sensor responses to lactate and glucose to concentrations determined in the blood levels using commercial instruments for (A, B) subject #1 (based on data reported in Fig. 7B) and (C, D) subject #2 (based on data reported in Fig. S11).

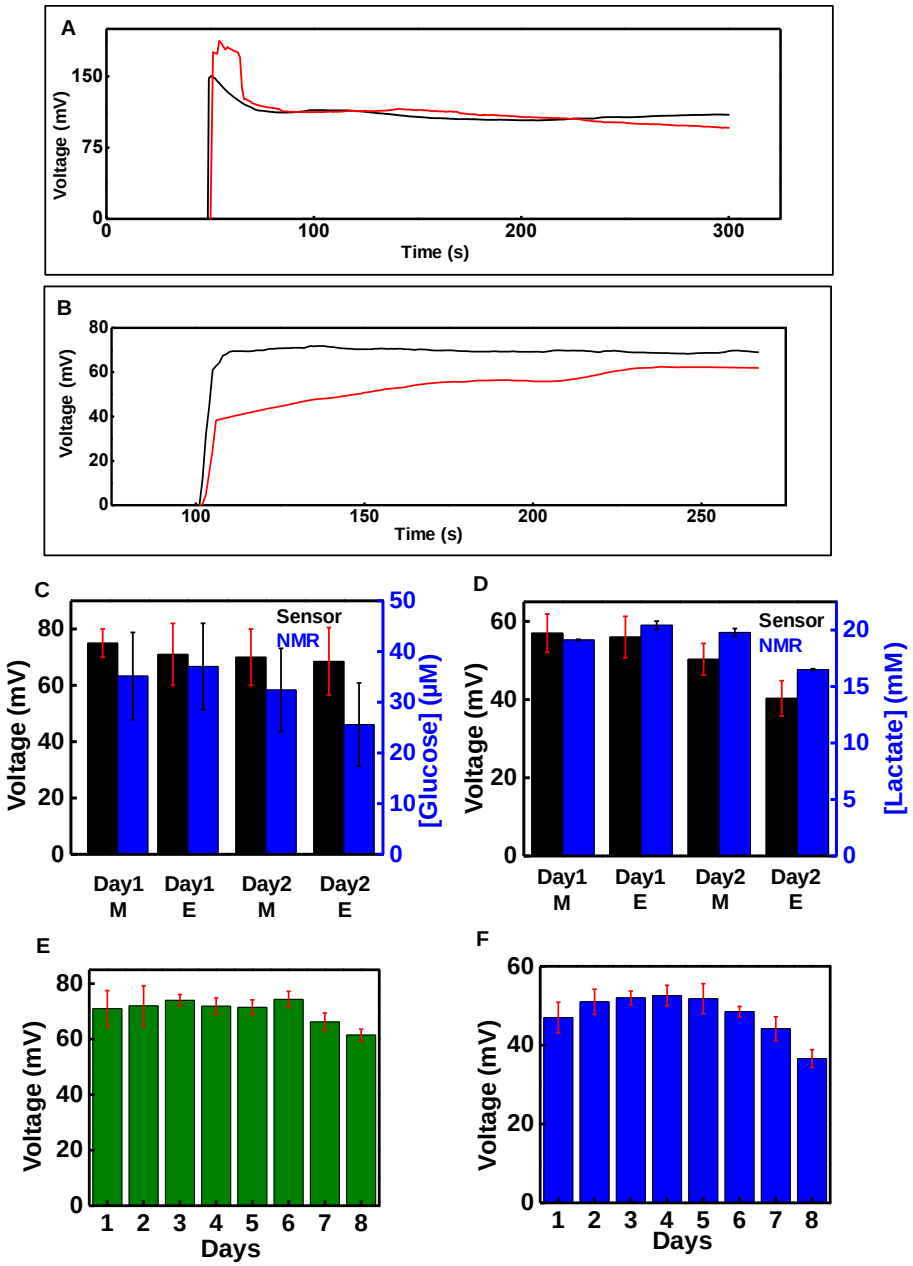

Fig. S13. (A) Comparison of signal of fresh, unused glucose sensor (black) with that obtained from one after two-day human trial (red) when exposed to 300μM glucose solution. (B) Comparison of signal of fresh, unused lactate sensor (black) with that obtained from one after two-day human trial (red) when exposed to 10mM lactate solution. Two-day human trails study comparing sweat sensor signals with that from NMR for (C) glucose and (D) lactate. (M: morning; E: evening). Benchtop stability studies of (E) glucose (100 μM) and (F) lactate (5 mM) sensors using artificial sweat at a temperature 30 ± 3 °C with the device bent to a radius of curvature of 35 mm.

	Lactate			Glucose		
Sr. No.	**Sensitivity**	**LOD**	**Ref**	**Sensitivity**	**LOD**	**Ref**
1	2.3 $\mu A \mu M^{-1} cm^{-2}$	1.47 mM	20	0.16 $\mu A \mu M^{-1} cm^{-2}$	11.92 µM	20
2	6 $\mu A \mu M^{-1} cm^{-2}$	0.7 mM	23	0.1 $\mu A \mu M^{-1} cm^{-2}$	10 µM	25
3	1.84 $\mu A \mu M^{-1} cm^{-2}$	5.1 nM	12	0.01 $\mu A \mu M^{-1} cm^{-2}$	20 µM	27
4	124 $mV mM^{-1} cm^{-2}$	2.1 mM	Present work	5.4 $mV \mu M^{-1} cm^{-2}$	43 µM	Present work

Table S1. Comparison of sensitivity and LOD for lactate and glucose sensor with that for previous examples.

Subject	Parameter	Hybrid Sensor Patch	Conventional Technique
#1	Chloride	62 ± 5mM	66 mM
		36 ± 5mM	43 mM
	pH	6.3 ± 0.05	6
		6.2 ± 0.03	5.5
	Lactate	10.4 ± 0.1 mM	17.5 mM
	Glucose	23.2 ± 2.4 µM	53 µM
#2	Chloride	34 ± 2mM	40 mM
	pH	6.4 ± 0.1	6.5
	Lactate	19.3 ± 0.5 mM	28 mM
	Glucose	52 ± 14 µM	100 µM

Table S2. Comparison of data acquired from sensor patch and conventional techniques during human trials.